

This is a repository copy of *Single-Organelle Quantification Reveals Stoichiometric and Structural Variability of Carboxysomes Dependent on the Environment*.

White Rose Research Online URL for this paper:

<https://eprints.whiterose.ac.uk/145727/>

Version: Accepted Version

---

**Article:**

Sun, Yaqi, Wollman, Adam [orcid.org/0000-0002-5501-8131](https://orcid.org/0000-0002-5501-8131), Huang, Fang et al. (2 more authors) (2019) *Single-Organelle Quantification Reveals Stoichiometric and Structural Variability of Carboxysomes Dependent on the Environment*. *The Plant Cell*. pp. 1648-1664. ISSN 1532-298X

<https://doi.org/10.1105/tpc.18.00787>

---

**Reuse**

Items deposited in White Rose Research Online are protected by copyright, with all rights reserved unless indicated otherwise. They may be downloaded and/or printed for private study, or other acts as permitted by national copyright laws. The publisher or other rights holders may allow further reproduction and re-use of the full text version. This is indicated by the licence information on the White Rose Research Online record for the item.

**Takedown**

If you consider content in White Rose Research Online to be in breach of UK law, please notify us by emailing [eprints@whiterose.ac.uk](mailto:eprints@whiterose.ac.uk) including the URL of the record and the reason for the withdrawal request.

1 RESEARCH ARTICLE

2  
3 **Single-Organelle Quantification Reveals Stoichiometric and Structural**  
4 **Variability of Carboxysomes Dependent on the Environment**

5  
6 **Yaqi Sun<sup>1†</sup>, Adam J. M. Wollman<sup>2†</sup>, Fang Huang<sup>1</sup>, Mark C. Leake<sup>2\*</sup>, Lu-Ning Liu<sup>1\*</sup>**

7  
8 <sup>1</sup> Institute of Integrative Biology, University of Liverpool, Liverpool L69 7ZB, United Kingdom

9 <sup>2</sup> Biological Physical Sciences Institute, Departments of Physics and Biology, University of York, YO10  
10 5DD, United Kingdom

11  
12 † These authors contributed equally to this work.

13 \* Corresponding authors:

14 **Mark C. Leake**, Tel.: +44 (0)190 432 2697, Email: mark.leake@york.ac.uk

15 **Lu-Ning Liu**, Tel.: +44 (0)151 795 4426, Email: luning.liu@liverpool.ac.uk

16  
17 **Short title:** Carboxysome protein stoichiometry and variability

18  
19 **One Sentence Summary:** Determination of absolute protein stoichiometry reveals the organizational  
20 variability of carboxysomes in response to microenvironmental changes

21  
22 The authors responsible for distribution of materials integral to the findings presented in this article in  
23 accordance with the policy described in the Instructions for Author ([www.plantcell.org](http://www.plantcell.org)) is: Lu-Ning Liu  
24 ([luning.liu@liverpool.ac.uk](mailto:luning.liu@liverpool.ac.uk)).

25  
26 **ABSTRACT**

27 The carboxysome is a complex, proteinaceous organelle that plays essential roles in carbon  
28 assimilation in cyanobacteria and chemoautotrophs. It comprises hundreds of protein homologs that  
29 self-assemble in space to form an icosahedral structure. Despite its significance in enhancing CO<sub>2</sub>  
30 fixation and potentials in bioengineering applications, the formation of carboxysomes and their  
31 structural composition, stoichiometry and adaptation to cope with environmental changes remain  
32 unclear. Here we use live-cell single-molecule fluorescence microscopy, coupled with confocal and  
33 electron microscopy, to decipher the absolute protein stoichiometry and organizational variability of  
34 single β-carboxysomes in the model cyanobacterium *Synechococcus elongatus* PCC7942. We  
35 determine the physiological abundance of individual building blocks within the icosahedral  
36 carboxysome. We further find that the protein stoichiometry, diameter, localization and mobility  
37 patterns of carboxysomes in cells depend sensitively on the microenvironmental levels of CO<sub>2</sub> and  
38 light intensity during cell growth, revealing cellular strategies of dynamic regulation. These findings,  
39 also applicable to other bacterial microcompartments and macromolecular self-assembling systems,  
40 advance our knowledge of the principles that mediate carboxysome formation and structural  
41 modulation. It will empower rational design and construction of entire functional metabolic factories in  
42 heterologous organisms, for example crop plants, to boost photosynthesis and agricultural productivity.

43  
44 **Keywords**

45 Bacterial microcompartment, carboxysome, protein stoichiometry, self-assembly, single-molecule  
46 fluorescence imaging, structural flexibility

## 48 INTRODUCTION

49 Organelle formation and compartmentalization within eukaryotic and prokaryotic cells provide  
50 the structural foundation for segmentation and modulation of metabolic reactions in space and  
51 time. Bacterial microcompartments (BMCs) are self-assembling organelles widespread  
52 among bacterial phyla (Axen et al., 2014). By physically sequestering specific enzymes key  
53 for metabolic processes from the cytosol, these organelles play important roles in CO<sub>2</sub> fixation,  
54 pathogenesis, and microbial ecology (Yeates et al., 2010; Bobik et al., 2015). According to  
55 their physiological roles, three types of BMCs have been characterized: the carboxysomes for  
56 CO<sub>2</sub> fixation, the PDU microcompartments for 1,2-propanediol utilization, and the EUT  
57 microcompartments for ethanolamine utilization.

58

59 The common features of various BMCs are that they are ensembles composed of purely  
60 protein constituents and comprise an icosahedral single-layer shell that encases the catalytic  
61 enzyme core. This proteinaceous shell, structurally resembling virus capsids, is self-  
62 assembled from several thousand polypeptides of multiple protein paralogs that form  
63 hexagons, pentagons and trimers (Kerfeld and Erbilgin, 2015; Sutter et al., 2016; Faulkner et  
64 al., 2017). The highly-ordered shell architecture functions as a physical barrier that  
65 concentrates and protects enzymes, as well as selectively gating the passage of substrates  
66 and products of enzymatic reactions (Yeates et al., 2010; Bobik et al., 2015).

67

68 Carboxysomes serve as the key CO<sub>2</sub>-fixing machinery in all cyanobacteria and some  
69 chemoautotrophs. The primary carboxylating enzymes, ribulose-1,5-bisphosphate  
70 carboxylase oxygenase (Rubisco) (Rae et al., 2013), are encapsulated by the carboxysome  
71 shell that facilitates the diffusion of HCO<sub>3</sub><sup>-</sup> and probably reduces CO<sub>2</sub> leakage into the cytosol  
72 (Dou et al., 2008). Based on the form of enclosed Rubisco, carboxysomes can be categorized  
73 into two different classes, α-carboxysomes and β-carboxysomes (Rae et al., 2013; Kerfeld  
74 and Melnicki, 2016). The β-carboxysomes in the cyanobacterium *Synechococcus elongatus*  
75 PCC7942 (Syn7942) have been extensively characterized as the model carboxysomes. The  
76 shell of β-carboxysomes from Syn7942 is composed of the hexameric proteins CcmK2,  
77 CcmK3 and CcmK4 that form predominately the shell facets (Kerfeld et al., 2005), the  
78 pentameric protein CcmL that caps the vertices of the polyhedron (Tanaka et al., 2008), as  
79 well as the trimeric proteins CcmO and CcmP (Cai et al., 2013; Larsson et al., 2017). The  
80 core enzymes of β-carboxysomes consist of a paracrystalline arrangement of plant-type

81 Rubisco (comprising the large and small subunits RbcL and RbcS) and  $\beta$ -carbonic anhydrase  
82 ( $\beta$ -CA, encoded by the *ccaA* gene). The colocalized  $\beta$ -CA dehydrates  $\text{HCO}_3^-$  to  $\text{CO}_2$  and  
83 creates a  $\text{CO}_2$ -rich environment in the carboxysome lumen to favor the carboxylation of  
84 Rubisco. In addition, CcmM and CcmN function as “linker” proteins to promote Rubisco  
85 packing and shell-interior association (Kinney et al., 2012). CcmM in the  $\beta$ -carboxysome  
86 appears as two isoforms, a 35-kDa truncated CcmM35 and a full-length 58-kDa CcmM58  
87 (Long et al., 2007; Long et al., 2010; Long et al., 2011). CcmM35 contains three Rubisco  
88 small subunit-like (SSU) domains that interact with Rubisco (Hagen et al., 2018b; Wang et al.,  
89 2019), whereas CcmM58 has an N-terminal  $\gamma$ -CA-like domain in addition to the SSU domains  
90 and recruits CcaA to the shell. RbcX is recognized as a chaperonin-like protein for Rubisco  
91 assembly (Emlyn-Jones et al., 2006; Saschenbrecker et al., 2007; Occhialini et al., 2016); it  
92 has been recently revealed to serve as one component of the carboxysome and play roles in  
93 mediating carboxysome assembly and subcellular distribution (Huang et al., 2019).

94

95 Understanding the physiological composition and assembly principles of carboxysome  
96 building blocks is of key importance not solely to unravel the underlying molecular  
97 mechanisms of carboxysome formation and biological functions, but also for heterologously  
98 engineering and modulating functional  $\text{CO}_2$ -fixing organelles to supercharge photosynthetic  
99 carbon fixation in synthetic biology applications. Previous estimations of the carboxysome  
100 protein stoichiometry from either the whole cell lysates or the isolated forms using immunoblot  
101 and mass spectrometry illustrated the relative abundance of carboxysome proteins (Long et  
102 al., 2005; Long et al., 2011; Rae et al., 2012; Faulkner et al., 2017). Moreover, it was revealed  
103 that carboxysome biosynthesis in Syn7942 is highly dependent upon environmental  
104 conditions during cell growth, such as light intensity (Sun et al., 2016) and  $\text{CO}_2$  availability  
105 (McKay et al., 1993; Harano et al., 2003; Woodger et al., 2003; Whitehead et al., 2014). The  
106 exact stoichiometry of all building components in the functional carboxysome and how  
107 carboxysomes manipulate their compositions, organizations and functions to cope with  
108 environmental changes have remained elusive.

109

110 Here, we construct a series of Syn7942 mutants with individual components of carboxysomes  
111 functionally tagged with the bright and fast-maturing enhanced yellow fluorescent protein  
112 (YFP) and report the *in vivo* characterization of protein stoichiometry of carboxysomes at the  
113 single-organelle level, using real-time single-molecule fluorescence microscopy, confocal and

114 electron microscopy combined with a suite of biochemical and genetic assays. Quantification  
115 of the protein stoichiometry of  $\beta$ -carboxysomes in Syn7942 grown under different conditions  
116 demonstrates the organizational flexibility of  $\beta$ -carboxysomes, and their ability to modulate  
117 functions towards local alterations of CO<sub>2</sub> levels and light intensity during cell growth, as well  
118 as the regulation of the spatial localization and mobility of  $\beta$ -carboxysomes in the cell. This  
119 study provides fundamental insight into the formation and structural plasticity of  
120 carboxysomes and their dynamic organization towards environmental changes, which could  
121 be extended to other BMCs and macromolecular systems. A deeper understanding of the  
122 protein composition and structure of carboxysomes will inform strategies for rational design  
123 and engineering of functional and adjustable metabolic modules towards biotechnological  
124 applications.

125

126

127 **RESULTS**

128 **Protein stoichiometry of functional carboxysomes at the single-organelle level**

129 We constructed ten Syn7942 strains expressing individual  $\beta$ -carboxysome proteins (CcmK3,  
130 CcmK4, CcmK2, CcmL, CcmM, CcmN, RbcL, RbcS, CcaA, RbcX) fused with YFP at their C-  
131 termini individually (Supplemental Figure 1). Fluorescence tagging at the native chromosomal  
132 locus under the control of their native promoters ensures expression of the fluorescently-  
133 tagged proteins in context and at physiological levels (Sun et al., 2016). Eight of these strains,  
134 in which YFP was fused to CcmK3, CcmK4, CcmL, CcmM, CcmN, RbcS, CcaA, and RbcX  
135 respectively, are fully segregated (Supplemental Figures 1C and 2) and exhibit wild-type  
136 levels of cell size, growth and carbon fixation within experimental error (Supplemental Table  
137 1), consistent with previous observations (Savage et al., 2010; Cameron et al., 2013; Sun et  
138 al., 2016; Faulkner et al., 2017; Huang et al., 2019).

139  
140 By contrast, RbcL-YFP and CcmK2-YFP strains are only partially segregated, in agreement  
141 with previous studies (Savage et al., 2010; Cameron et al., 2013; Sun et al., 2016). Through  
142 immunoblot analysis using anti-fluorescence protein, anti-RbcL and anti-CcmK2 antibodies  
143 (Supplemental Figure 2B), we estimate that  $29.2 \pm 7.1$  % (mean  $\pm$  standard deviation (SD),  $n$   
144 = 4) of total RbcL and  $6.0 \pm 0.7$  % ( $n = 3$ ) of total CcmK2 were tagged with YFP in RbcL-YFP  
145 and CcmK2-YFP strains. Nevertheless, we excluded the stoichiometric quantification of RbcL  
146 and CcmK2 in this study, in view of the partial segregation which could result in quantification  
147 inaccuracy.

148  
149 We used single-molecule Slimfield microscopy (Plank et al., 2009) to visualize individual  
150 carboxysomes that were fused with YFP (Figure 1, Supplemental Figure 3). This technique  
151 allows detection of fluorescently-labelled proteins with millisecond sampling, enabling real-  
152 time tracking of rapid protein dynamics inside living cells, exploited previously to study  
153 functional proteins involved in bacterial DNA replication and remodeling (Reyes-Lamothe et  
154 al., 2010; Badrinarayanan et al., 2012), gene regulation in budding yeast cells (Wollman et al.,  
155 2017; Leake, 2018), bacterial cell division (Lund et al., 2018), and chemokine signaling in  
156 lymph nodes (Miller et al., 2018). Our prior measurements using relatively fast-maturing  
157 fluorescent proteins such as YFP suggest that less than 15% of fluorescent proteins are likely  
158 to be in a non-fluorescent immature state (Leake et al., 2008; Shashkova et al., 2018).

159

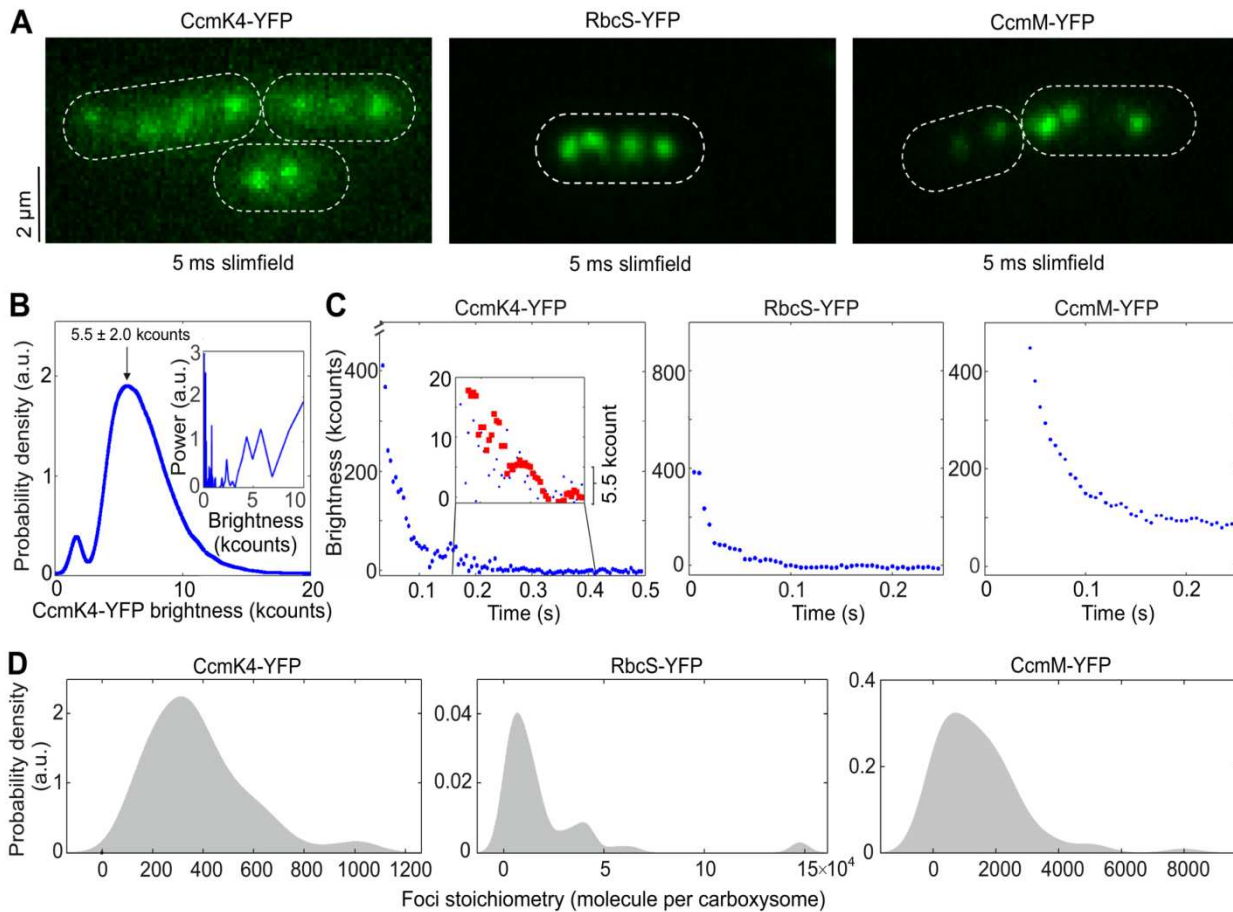


**Figure 1. Slimfield quantification of cells grown under ambient air/moderate light Air/ML condition.**

**(A)** Averaged Slimfield images of YFP fluorescence (green) over 5 frames of strains expressing shell component CcmK4-YFP, the interior enzyme RbcS-YFP and the shell-interior linker protein CcmM-YFP. White dash lines indicate cell body outlines.

**(B)** Distribution of automatically detected foci intensity from the end of the photobleaching, corresponding to the characteristic intensity of *in vivo* YFP. Inset shows the Fourier spectrum of ‘overtracked’ foci, tracked beyond photobleaching, showing a peak at the characteristic intensity.

**(C)** Representative fluorescence photobleaching tracked at ultra-fast speed. The CcmK4 plot shows an inset ‘zoomed in’ on lower intensity range with step-preserving Chung-Kennedy filtered data in red, with individual photobleaching steps clearly visible at the characteristic intensity. Brightness (kcounts), counts measured per camera pixel multiplied by 1,000.

**(D)** Distribution of YFP copy number detected for individual carboxysomes in corresponding mutants, rendered as kernel density estimates using standard kernel width. Heterogeneity of contents was observed, also a “preferable” copy number, represented by kernel density peak values could be determined. Statistics of copy numbers (Peak value  $\pm$  HWHM) are listed in Table 1 for ML conditions. The corresponding Slimfield images and histogram for complete strain sets are shown in Supplemental Figure 3.

160 Figure 1A shows the Slimfield images of three representative Syn7942 strains RbcS-YFP,  
 161 CcmK4-YFP and CcmM-YFP that grow under ambient air and moderate light (hereafter

162 denoted Air/ML), to determine the protein stoichiometry from different carboxysome structural  
163 domains. Single carboxysomes are detected as distinct fluorescent foci in cells of the YFP-  
164 fused strains (Figure 1A, Supplemental Figure 3), whose sigma width is approximately 250  
165 nm ( $n = 100$ ), comparable to the diffraction-limited point spread function width of our imaging  
166 system. We use the number of YFP molecules per fluorescent focus as an indicator of the  
167 stoichiometry of the fluorescently-labelled protein subunits in each individual carboxysomes,  
168 which we determined by quantifying step-wise photobleaching of the fluorescent tag during  
169 the Slimfield laser excitation process (Figures 1B to 1C, Table 1) using a combination of  
170 Fourier spectral analysis and edge-preserving filtration of the raw data (Leake et al., 2003;  
171 Leake et al., 2004; Leake et al., 2006) (see details in Materials and Methods). The resulting  
172 broad distributions of protein stoichiometry, rendered as kernel density estimates, suggest a  
173 variable content of individual components per carboxysome (Figure 1D), indicative of the  
174 structural heterogeneity of  $\beta$ -carboxysomes. The modal average stoichiometry of each protein  
175 subunit per carboxysome was defined by the measured peak from each distribution of the raw  
176 stoichiometric data (Figure 1D, Supplemental Figure 3), after subtracting the background  
177 fluorescence distribution, primarily from chlorophylls, which was determined from the WT cells  
178 (Supplemental Figure 4).

179

180 In the  $\beta$ -carboxysome synthesized in cells grown under Air/ML, Rubisco enzymes are the  
181 predominant components, as indicated by the RbcS content (Table 1). CcmM is the second  
182 most abundant element; there are over 700 copies of CcmM molecules per  $\beta$ -carboxysome.  
183 In addition, the CcmK4 content is greater than that of CcmK3 by a factor of 3.8. CcmL, CcmN,  
184 CcaA and RbcX are the minor components in the  $\beta$ -carboxysome. Our results reveal that  
185 there are 37 CcmL subunits per carboxysome, with the raw stoichiometry distribution showing  
186 some indications of peaks at multiples of  $\sim 5$  molecules indicative of multiples of CcmL  
187 pentamers (Supplemental Figure 4C), consistent with the atomic structure of CcmL (Tanaka  
188 et al., 2008). A modal average of 37 CcmL molecules thus suggests that a single  
189 carboxysome contains an average of 7.4 CcmL pentamers, less than the 12 CcmL pentamers  
190 that were postulated to occupy all the vertices of the icosahedral shell (Bobik et al., 2015;  
191 Kerfeld et al., 2018). It is feasible that not all vertices of the carboxysome structure are  
192 capped by CcmL pentamers, as BMC shells deficient in pentamers could still be formed  
193 without notable structural variations (Cai et al., 2009; Lassila et al., 2014; Hagen et al., 2018a).



194 Our study represents a direct characterization of protein stoichiometry at the level of single  
195 functional carboxysomes in their native cellular environment.

196

197 As a control, we fused RbcL with mYPet, a monomeric-optimized variant of YFP. The RbcL-  
198 YFP and RbcL-mYPet cells show no significant difference in the subcellular distribution of  
199 carboxysomes as well as cell doubling times and carbon fixation (Supplemental Figure 5),  
200 demonstrating that there are no measurable artefacts due to putative effects of dimerization of  
201 the YFP tag.

202

203 We also examined the relative abundance of individual carboxysome proteins in the YFP-  
204 fusion Syn7942 strains in cell lysates, using immunoblot probing with an anti-fluorescent  
205 protein antibody (Supplemental Figure 2A, Supplemental Table 2). To compare with the  
206 stoichiometry obtained from Slimfield, we normalized the abundance of carboxysome proteins  
207 estimated from immunoblot analysis, using the RbcS content per carboxysome determined by  
208 Slimfield. It appears that the content of  $\beta$ -carboxysome proteins determined by  
209 immunoblotting is generally greater than that within the carboxysome characterized by  
210 Slimfield. Despite the potential effects caused by YFP fusion, this could suggest the presence  
211 of a “storage pool” of carboxysome proteins located in the cytoplasm that are involved in the  
212 biogenesis, maturation and turnover of carboxysomes. The ratio of RbcL/S detected from cell  
213 lysates fraction is about 8:5.8 ( $n = 4$ ) (Supplemental Table 2), in line with previous results  
214 (Long et al., 2011) but distinct from the *in vitro* reconstitution observations (Ryan et al., 2018;  
215 Wang et al., 2019).

216

### 217 **Stoichiometry of carboxysome proteins exhibit a dependence on the** 218 **microenvironment conditions of live cells**

219 Our previous study showed that the content and spatial positioning of  $\beta$ -carboxysomes in  
220 Syn7942 are dependent upon light intensity during cell growth, revealing the physiological  
221 regulation of carboxysome biosynthesis (Sun et al., 2016). Whether the stoichiometry of  
222 different components in the carboxysome structure changes in response to fluctuations in  
223 environmental conditions is unknown. Here we addressed this question by taking advantage  
224 of the far greater throughput of confocal microscopy compared to Slimfield, whilst still using  
225 the single-molecule precise Slimfield data as a calibration to convert the intensity of detected  
226 foci from confocal images into estimates for absolute numbers of stoichiometry. We achieved

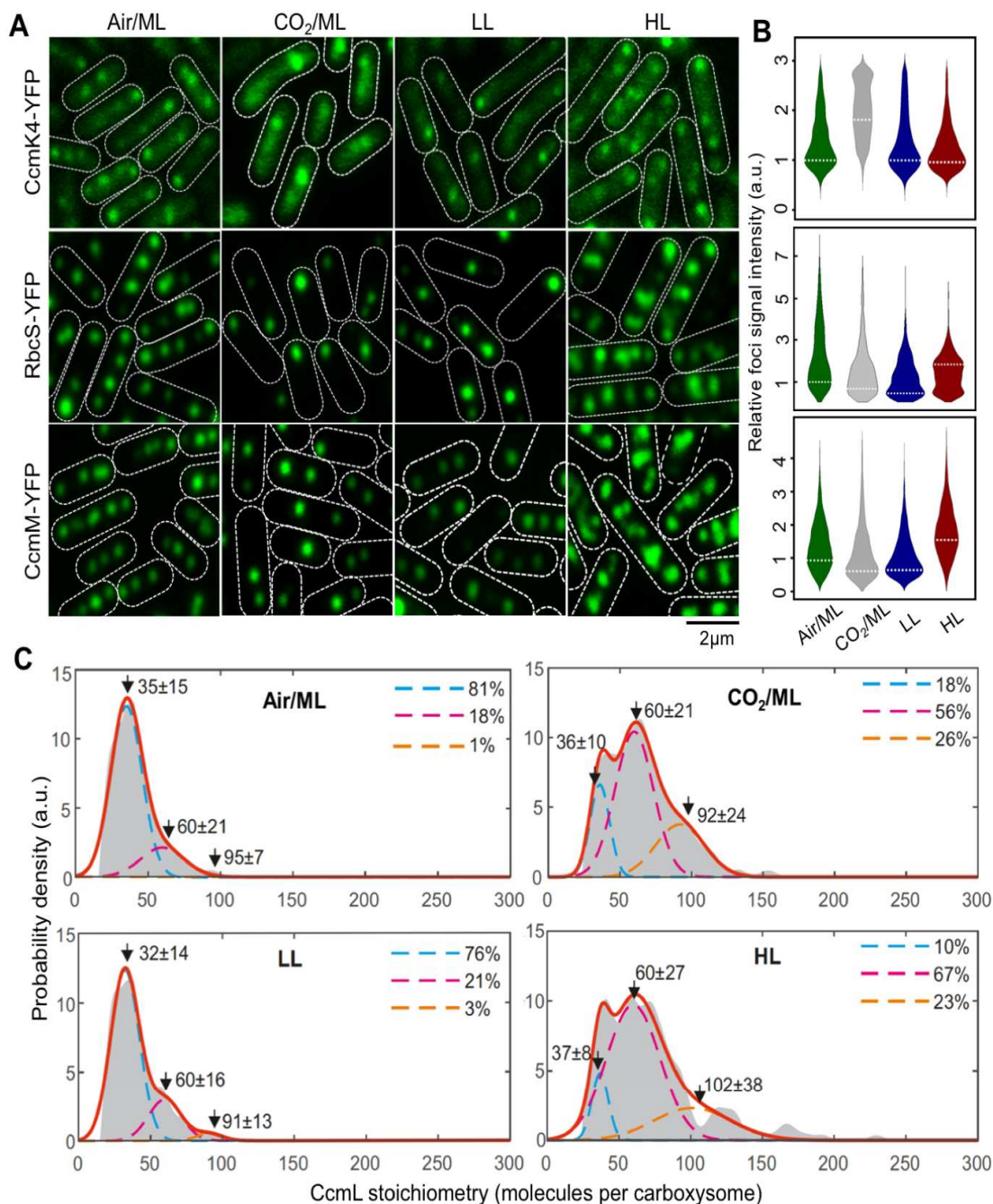


**Figure 2. Relative protein quantification of CcmK4, RbcS and CcmM in the carboxysome under different CO<sub>2</sub> levels and light intensities using confocal microscopy.**

**(A)** Confocal images of CcmK4-YFP, RbcS-YFP and CcmM-YFP strains under Air/ML, CO<sub>2</sub>/ML, LL and HL. Fluorescence foci (green) indicate carboxysomes and cell borders were outlined by white dashed lines. Scale bar indicates 2 μm.

**(B)** Violin plot of carboxysome intensities under Air/ML, CO<sub>2</sub>/ML, LL and HL, normalized to kernel density ML peak values (peaks marked by white dash lines).

**(C)** Kernel density estimates of CcmL carboxysome copy number grown under Air/ML, CO<sub>2</sub>, LL and HL detected by Slimfield and corrected for chlorophyll. Triple Gaussian fits are indicated as colored dashed lines with summed fit in red. The percentage in each Gaussian is indicated aside.

228 obtained from confocal imaging with the peak value of the measured Slimfield foci  
229 stoichiometry distribution for the equivalent cell strain under Air/ML. This approach allows us  
230 to generate a conversion factor which we then applied to subsequent confocal data acquired  
231 under lower light (LL), higher light (HL) and ML with the air supplemented by 3% CO<sub>2</sub>, and to  
232 estimate relative changes in the stoichiometry of carboxysome building components using  
233 large numbers of cells, without the need to obtain separate Slimfield datasets for each  
234 condition (Figure 2, Supplemental Figures 6 to 8).

235

236 Figure 2A shows confocal fluorescence images of RbcS-YFP, CcmK4-YFP, and CcmM-YFP  
237 strains grown under Air/ML, 3% CO<sub>2</sub> (CO<sub>2</sub>/ML), LL and HL. The confocal images reveal  
238 classic patterns of cellular localization of carboxysomes similar to those observed with  
239 Slimfield microscopy (Supplemental Figure 6). We analyzed the confocal images to detect  
240 carboxysome fluorescent foci within the cells and quantify their fluorescence intensities  
241 (Figure 2B, Supplemental Figures 7 and 8). We find that the number of carboxysomes per cell  
242 is dependent on growth conditions: it is reduced under CO<sub>2</sub>/ML in contrast to Air/ML, whereas  
243 HL increases the abundance of  $\beta$ -carboxysomes (Supplemental Table 3), consistent with  
244 previous findings (Whitehead et al., 2014; Sun et al., 2016). The slightly different  
245 carboxysome contents estimated in individual YFP-fused strains might suggest potential  
246 mechanisms of the cells that tune carboxysome organization. As a common feature, the  
247 abundance of all the proteins in the  $\beta$ -carboxysome is apparently modulated under distinct  
248 growth conditions. For instance, both RbcS and CcmM have a higher content per  
249 carboxysome under HL compared with that under other conditions, whereas the CcmK4  
250 content per  $\beta$ -carboxysome increase under 3% CO<sub>2</sub> (Figure 2B). The dependence of  
251 carboxysome protein stoichiometry inferred from the peak values of the stoichiometry  
252 distributions under different cellular microenvironmental conditions is summarized in Table 1.

253

254 Interestingly, we find that the variation of CcmL abundance per carboxysome rises with  
255 increasing light illumination and CO<sub>2</sub> availability (Figure 2C). The measured stoichiometry  
256 distribution of CcmL pentamers suggests the presence of three populations: (I) carboxysomes  
257 with < 60 CcmL subunits (in the range of 32-37); (II) carboxysomes with 60 CcmL subunits,  
258 consistent with the expectation that 12 vertices of the icosahedral carboxysome are fully  
259 occupied by CcmL pentamers (Tanaka et al., 2008; Rae et al., 2013; Kerfeld et al., 2018); (III)  
260 carboxysomes with > 60 CcmL subunits (in the range of 91-102). Using a nearest-neighbor

261 model to estimate the probability for the diffraction-limited optical images of individual  
262 carboxysomes in a cell, we find that the Population III carboxysomes represent random  
263 overlap of two or more carboxysomes from the Population I and II (Figure 2C). Population I  
264 represents a “non-complete capped” state in which not all vertices in the icosahedron are  
265 occupied by CcmL pentamers. We find the characteristic stoichiometry of the Population I  
266 carboxysomes increases with the enhancement of light intensity during cell growth, from 32  
267 CcmL molecules (LL) to 35 (ML) and 37 (HL), with HL having a significantly smaller proportion  
268 (23%) of “non-complete capped” carboxysomes compared to ~80% under LL and ML  
269 conditions. Supplementing the air with 3% CO<sub>2</sub> under ML similarly results in a substantial  
270 decrease in the proportion of “non-complete capped” carboxysomes in the population (18%)  
271 comparable to the HL condition in the absence of any supplemental CO<sub>2</sub>. These findings  
272 suggest a dependence of carboxysome assembly which may allow adaptation towards  
273 microenvironmental changes, i.e. the increase in the population of capped carboxysomes in  
274 situations which are favorable towards photosynthesis (HL conditions and locally-raised levels  
275 of CO<sub>2</sub>).

276

277 This finding is also validated by the changes in protein abundance of other carboxysome  
278 components under environmental regulation (Table 1, Supplemental Figures 7 and 8). Cells  
279 were maintained under different growth conditions prior to microscopy imaging, to ensure  
280 their full acclimation. Variations of protein content in carboxysomes under CO<sub>2</sub>/ML vs. Air/ML,  
281 and HL vs. LL conditions indicate distinct fashions of stoichiometric regulation of  
282 carboxysome building blocks (Figure 3, Supplemental Table 4). The abundance of CcmK3  
283 and CcmK4, whose encoding genes are distant from the *ccmKLMNO* operon (Sommer et al.,  
284 2017), increases under 3% CO<sub>2</sub> and remains relatively constant under HL/LL, contrary to the  
285 changes in the abundance of CcmN and CcmM that are located in the *ccm* operon. In  
286 addition, the ratio of CcmK4:CcmK3 per carboxysome appear to be relatively constant, in the  
287 range of 3.6–4.1 (Supplemental Table 5), indicating the organizational correlation between  
288 CcmK3 and CcmK4 within the β-carboxysome structure. We find the rise of CcaA content and  
289 reduction of RbcS content under CO<sub>2</sub>/ML vs. Air/ML, whereas both increase under HL,  
290 suggesting distinct regulation of the two components. It has been recently demonstrated that  
291 the putative Rubisco chaperone RbcX is part of the carboxysome and plays roles in mediating  
292 carboxysome formation (Huang et al., 2019). The fold changes of RbcX content in each  
293 carboxysome under different conditions are close to 1 (Figure 3), probably ascribed to the fact

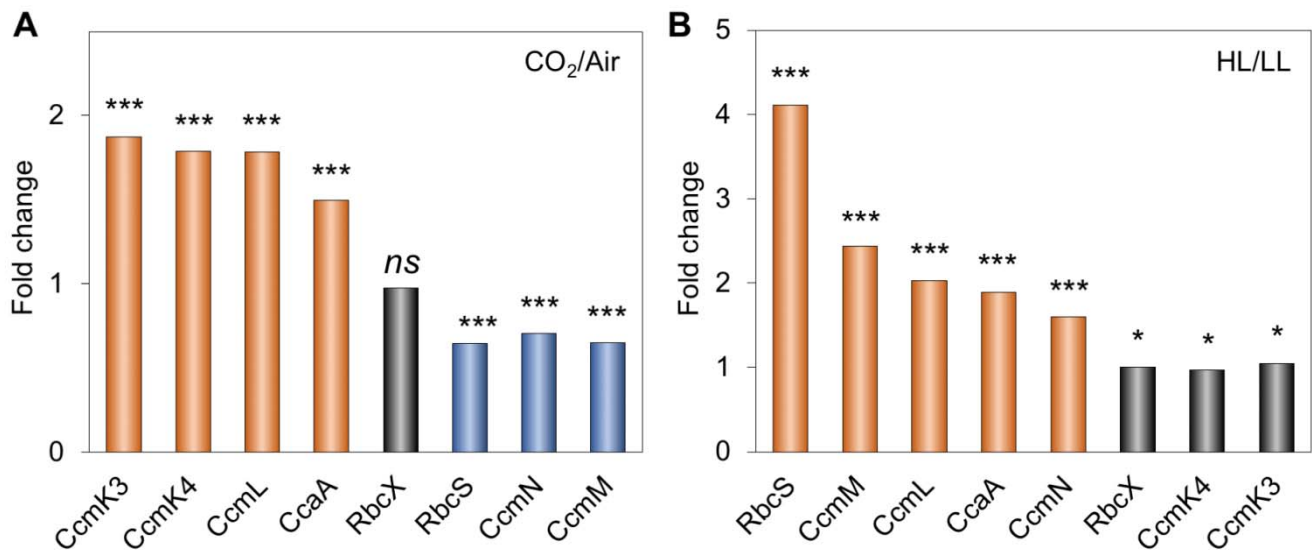


**Figure 3. Changes in carboxysome protein stoichiometry by increase in  $CO_2$  levels and light intensity.**

**(A)** Comparison of carboxysome protein stoichiometry under  $CO_2$  treatment. Increase in the  $CO_2$  concentration resulted in the rise of CcmK3, CcmK4, CcaA and CcmL contents and the decline of RbcS, CcmN and CcmM contents.

**(B)** Comparison of carboxysome protein stoichiometry under light intensity treatment. Increased light intensity led to the elevation of RbcS, CcmM, CcmL, CcaA and CcmN contents, whereas the abundance of RbcX, CcmK3 and CcmK4 contents per carboxysome does not change dramatically.

Man-Whitney U-tests were performed to compare the numbers of functional units of individual carboxysome proteins changed from  $CO_2/ML$  to  $Air/ML$  (A) and from HL to LL (B). \*,  $p < 0.05$ ; \*\*\*,  $p < 0.005$ ; ns,  $p > 0.05$ .

294 that its encoding gene is distant from the *rubisco* and *ccm* operons in Syn7942. Collectively,  
 295 these results highlight the highly flexible stoichiometry of individual components within the  
 296 natural carboxysomes in response to environmental changes.

297

### 298 **Variation of carboxysome diameter represents a strategy for manipulating** 299 **carboxysome activity to adapt to environmental conditions**

300 The change in the protein content per carboxysome signifies the variation of  $\beta$ -carboxysome  
 301 size and organization among different cell growth conditions. Indeed, electron microscopy  
 302 (EM) of Syn7942 WT cells substantiates the variable structures of  $\beta$ -carboxysomes in  
 303 response to the changing environment (Figures 4A and 4B). The average diameter of  $\beta$ -  
 304 carboxysomes is  $192 \pm 41$  nm ( $n = 33$ ) in  $Air/ML$ ,  $144 \pm 24$  nm ( $n = 25$ ) in 3%  $CO_2$ ,  $151 \pm 22$   
 305 nm ( $n = 27$ ) in LL, and  $208 \pm 28$  nm ( $n = 51$ ) in HL (Figure 4B, Supplemental Table 5,  
 306 Supplemental Figure 9). These results reveal that both the  $CO_2$  level and light intensity can

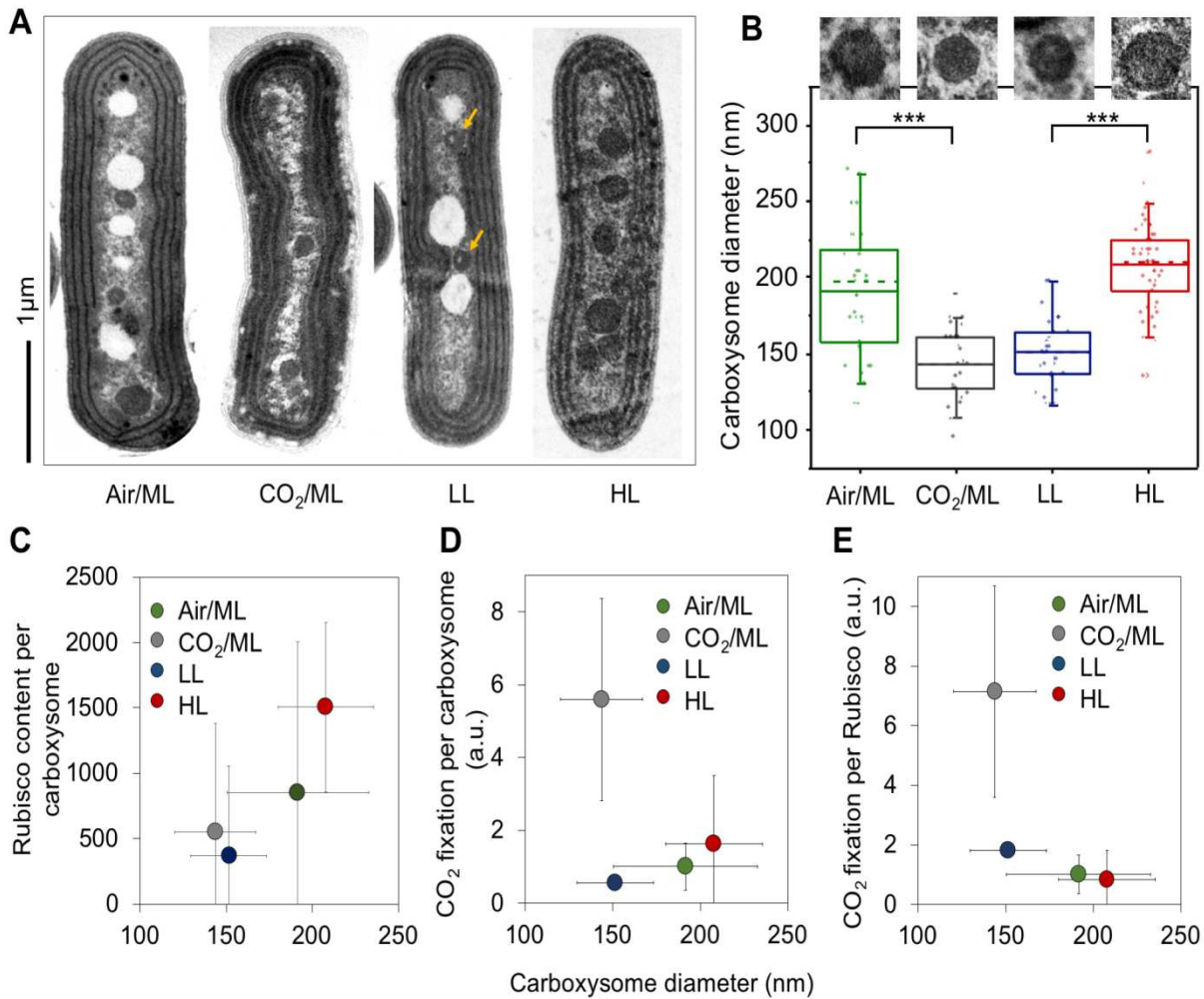


**Figure 4. Variations of the carboxysome size and carbon fixation under Air/ML, CO<sub>2</sub>, LL and HL.**

**(A)** Thin-section electron microscopy (EM) images showing individual carboxysomes in the Syn7942 WT cells under Air/ML, CO<sub>2</sub>, LL and HL treatments. Yellow arrows indicate the carboxysomes with spaces of low protein density under LL. More EM images are shown in Supplemental Figure 9. Scale bar indicates 1 μm.

**(B)** Changes in the carboxysome diameter under Air/ML, CO<sub>2</sub>, LL and HL measured from EM ( $n = 33, 25, 27$  and  $51$ , respectively), with representative carboxysome images depicted above. Dashed lines indicate medians and solid lines indicate means. Differences in the carboxysome diameter are significant between CO<sub>2</sub> and air ( $p = 1.92 \times 10^{-14}$ ) and between LL and HL ( $p = 8.29 \times 10^{-7}$ ), indicated as \*\*\*.

**(C)** Correlation between the carboxysome size and the Rubisco content per carboxysome under Air/ML, CO<sub>2</sub>, LL and HL.

**(D)** Correlation between the carboxysome size and CO<sub>2</sub> fixation per carboxysome.

**(E)** Correlation between the carboxysome size and CO<sub>2</sub> fixation per Rubisco of the carboxysomes. Carboxysome diameters and CO<sub>2</sub> fixation were present as average  $\pm$  SD, whereas the carboxysome total protein content and Rubisco content were shown as Peak value  $\pm$  HWHM.

307 result in alternations of carboxysome size (Figure 4B). Larger  $\beta$ -carboxysomes can

308 accommodate more Rubisco enzymes (estimated on the basis of RbcS content) (Figure 4C).  
309 An exception is the carboxysomes under LL, which are around 5% larger than the  
310 carboxysomes under 3% CO<sub>2</sub> but comprises only 67% of Rubisco per carboxysome under  
311 CO<sub>2</sub> (Figure 4C, Supplemental Table 5). EM images reveal that the lumen of β-carboxysomes  
312 synthesized under LL often contain regions with low protein density (Figure 4A, arrows;  
313 Supplemental Figure 9), 59% for LL (16 out of 27 carboxysomes) compared with 9% for  
314 Air/ML (3 out of 33), 12% for CO<sub>2</sub>/ML (3 out of 25) and 8% for HL (4 out of 51), which likely  
315 accounts for the reduced and uneven Rubisco loading within the β-carboxysome.

316

317 We also find that CO<sub>2</sub>-fixing activity per carboxysome increases as the β-carboxysome  
318 structure enlarges, which is correlated to strong light intensity during cell growth (Figure 4D),  
319 demonstrating the correlation between β-carboxysome structure and function *in vivo*.  
320 Moreover, under HL the CO<sub>2</sub>-fixation activity per Rubisco of the β-carboxysome declines as  
321 the carboxysome size and Rubisco density in the carboxysome lumen increase (Figure 4E,  
322 Supplemental Table 5). This may suggest that Rubisco density and local Rubisco packing are  
323 important for determining CO<sub>2</sub>-fixation activity of individual Rubisco (Supplemental Table 5).  
324 Interestingly, the relatively small β-carboxysomes under 3% CO<sub>2</sub> exhibit high CO<sub>2</sub>-fixing  
325 activities per Rubisco and per carboxysome, compared with β-carboxysomes under other  
326 conditions. The enhanced carbon fixation capacity under 3% CO<sub>2</sub> might be correlated with the  
327 increase in CcmK3 and CcmK4 content (Figure 3A, Table 1), as it has been shown that  
328 depletion of CcmK3/CcmK4 impedes carbon fixation of carboxysomes (Rae et al., 2012).

329

### 330 **Patterns of spatial localization and diffusion of β-carboxysomes in live cells change** 331 **dynamically depending upon light intensity during growth**

332 The patterns of β-carboxysome localization within the cyanobacterial cells appears to be  
333 crucial for carboxysome biogenesis and metabolic function (Savage et al., 2010; Sun et al.,  
334 2016). We measured the organizational dynamics of β-carboxysomes with distinct diameters  
335 in Syn7942 under different light intensities, using time-lapse confocal fluorescence imaging on  
336 the RbcL-YFP Syn7942 strain. Previous studies have shown that tagging of RbcL with  
337 fluorescent proteins does not obstruct β-carboxysome assembly and function in Syn7942  
338 (Savage et al., 2010; Cameron et al., 2013; Chen et al., 2013; Sun et al., 2016). During time-  
339 lapse confocal imaging, we applied illumination on the cell samples, similar to that used for  
340 cell growth, in order to maintain cell physiology. We find that the overall mobility of individual

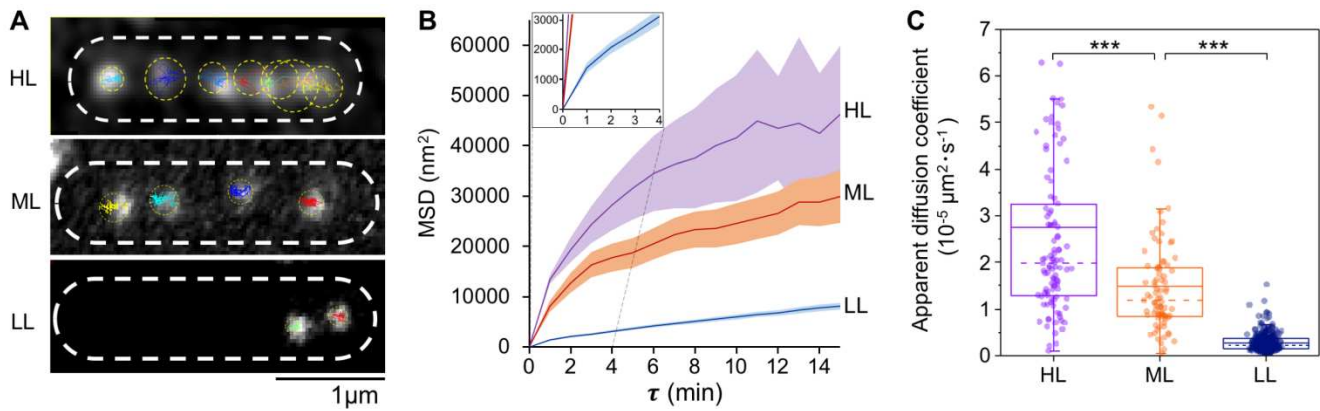


**Figure 5. Spatial localization and diffusion dynamics of carboxysomes in Syn7942 cells are dependent on light intensity.**

**(A)** Tracking of carboxysome diffusion in cells grown under HL, ML and LL. Colored lines indicate the diffusion trajectories of each carboxysomes and circles represent the diffusion areas of each carboxysomes over 60 mins. Scale bar indicates 1  $\mu\text{m}$ .

**(B)** Non-linear MSD (Mean Square Displacement) vs. the time interval ( $\tau$ ) profiles suggest the mobility of carboxysomes in Syn7942 cells grown under HL, ML and LL. Inset, zoom-in view of the MSD profile under LL.

**(C)** Diffusion coefficient of carboxysomes *in vivo* decreases significantly when the light intensity reduces:  $2.76 \pm 2.83 \times 10^{-5} \mu\text{m}^2 \cdot \text{s}^{-1}$  for HL (mean  $\pm$  SD,  $n = 105$ ),  $1.48 \pm 1.03 \times 10^{-5} \mu\text{m}^2 \cdot \text{s}^{-1}$  for ML ( $n = 84$ ), and  $0.28 \pm 0.19 \times 10^{-5} \mu\text{m}^2 \cdot \text{s}^{-1}$  for LL ( $n = 336$ ).  $p = 3.05 \times 10^{-5}$  between HL and ML;  $p = 2.77 \times 10^{-5}$  between ML and LL, two-tailed Student's t-test).

341  $\beta$ -carboxysomes within cyanobacterial cells is non-Brownian (Figure 5A, Supplemental Movie  
 342 1). Carboxysomes under HL display larger diffusive regions than those under LL. The mean  
 343 square displacement (MSD) of tracked carboxysomes increased with the rise of light intensity  
 344 (Figure 5B), as did the mean microscopic diffusion coefficient of individual carboxysomes  
 345 (Figure 5C): an average diffusion coefficient of  $2.76 \pm 2.83 \times 10^{-5} \mu\text{m}^2 \cdot \text{s}^{-1}$  for HL (mean  $\pm$  SD,  
 346  $n = 105$ ),  $1.48 \pm 1.03 \times 10^{-5} \mu\text{m}^2 \cdot \text{s}^{-1}$  for ML ( $n = 84$ ), and  $0.28 \pm 0.19 \times 10^{-5} \mu\text{m}^2 \cdot \text{s}^{-1}$  for LL ( $n =$   
 347 336). It is interesting that the mobility of carboxysomes does not exhibit typical constrained  
 348 diffusion – asymptotic MSD values at higher values of  $\tau$  (Robson et al., 2013) – but rather  
 349 exhibits anomalous diffusion at higher values of  $\tau$  characterized by a non-linear relation,  
 350 which can be observed in the intracellular protein mobility traces of other cellular systems  
 351 (Lenn et al., 2008; Wollman et al., 2017). These results indicate the intracellular restrictions,  
 352 for example the proposed interactions with the cytoskeletal system (Savage et al., 2010),  
 353 McdA and McdB (MacCready et al., 2018) and ParA-mediated chromosome segregation (Jain  
 354 et al., 2012), may mediate carboxysome positioning, but do not completely confine the  
 355 mobility of carboxysomes. Notably, carboxysomes with a larger diameter (Figure 4) generated



356 under HL present a higher diffusion coefficient compares with carboxysomes with relatively  
357 smaller size under ML and LL. However, there is no apparent correlation between the  
358 diffusion coefficient of carboxysomes and their size in the same light conditions  
359 (Supplemental Figure 10).

360

361

## 362 **Discussion**

363 Precise quantification of the protein stoichiometry and organizational regulation of  
364 carboxysomes provides insight into their assembly principles, structure and function. In this  
365 work, we functionally fused fluorescent protein tags to the building blocks in  $\beta$ -carboxysomes  
366 and exploited advanced “Physics of Life” technologies, in particular using bespoke single-  
367 molecule fluorescence microscopy to count the actual protein stoichiometry of  $\beta$ -  
368 carboxysomes in Syn7942 cells, at the single-organelle level. This approach minimizes the  
369 ensemble averaging encountered in bulk estimations from proteomic and immunoblot  
370 analysis. We characterized the stoichiometric flexibility of carboxysome proteins within  
371 individual polyhedral structures towards environmental variations. Variability of the protein  
372 stoichiometry and size of carboxysomes likely provides the structural foundation for the  
373 physiological regulation of carboxysome formation and carbon fixation activity. Given the  
374 shared structural features of carboxysomes and other BMCs, we believe that this work opens  
375 up new opportunities to quantitatively evaluate protein abundance and decipher the formation  
376 of all BMC organelles, in both native forms and synthetic variants.

377

378 Despite prior efforts on understanding carboxysome structure and function, the relative  
379 stoichiometry of functional carboxysome components in their native cell environment – key  
380 information required for reconstituting entire active carboxysome structures in synthetic  
381 biology (Fang et al., 2018), was still unclear. The major challenges have been the poor  
382 specificity of immunoblots and mass spectrometry, given the homology of carboxysome  
383 proteins and the lack of effective purification of intact carboxysomes from host cells, as well  
384 as the heterogeneity of carboxysome structures (Long et al., 2005). The previous model of  
385 carboxysome protein stoichiometry was based on the total amount of proteins in cell lysates  
386 (Long et al., 2011) and does not directly reflect the stoichiometry of carboxysome proteins in  
387 the organelle, given the possible free-standing carboxysome components in the cytosol (Dai  
388 et al., 2018). We have recently reported the isolation of  $\beta$ -carboxysomes from Syn7942 and  
389 the structural and mechanical exploration of the organelles (Faulkner et al., 2017).  
390 Interestingly, some components, i.e. CcmO, CcmN, CcmP and RbcX, were not detectable by  
391 mass spectrometry in the isolated carboxysomes, likely due to their low content or potential  
392 loss of carboxysome components during isolation. Here, as demonstrated, fluorescence  
393 tagging and Slimfield and confocal imaging enable single-organelle analysis of the protein  
394 stoichiometry of eight  $\beta$ -carboxysome proteins (including RbcX) and their regulation in their

395 native context, and extends analyses of the assembly and action of carboxysomes.  
396 Microscopy imaging of fluorescently-tagged  $\beta$ -carboxysomes has been used to reveal their  
397 patterns of cellular localization, biogenesis pathways and light-dependent regulation in  
398 Syn7942 (Savage et al., 2010; Cameron et al., 2013; Chen et al., 2013; Sun et al., 2016;  
399 Niederhuber et al., 2017; MacCready et al., 2018). Although we cannot completely exclude  
400 the potential effects of YFP tags on carboxysome structure, we validate that YFP tagging to  
401 most of the structural components does not impede formation of functional carboxysome  
402 structures, suggesting the physiological relevance of the determined protein stoichiometry in  
403 the carboxysome in the presence of fluorescence tags. This flexibility emphasizes the  
404 extraordinary capacity of the carboxysome structure in adjusting their protein stoichiometry  
405 and accommodating foreign proteins while maintaining functionality, indicating the possibility  
406 of manipulating carboxysome organization in bioengineering for diverse purposes.  
407 Exceptionally, fluorescence tagging on CcmP and CcmO does not show normal carboxysome  
408 assembly and localization compared to other YFP-tagged strains (Supplemental Figure 11).  
409 In this work, therefore, we did not include estimation of the protein abundance of CcmP and  
410 CcmO, as well as RbcL and CcmK2 that cannot be fully tagged with YFP.

411  
412 Numerous studies have described the regulation of carboxysome protein expression at the  
413 transcriptional level (McGinn et al., 2003; Woodger et al., 2003; Schwarz et al., 2011).  
414 Counting protein abundance of  $\beta$ -carboxysomes at different cell growth conditions enables  
415 direct characterization of the stoichiometric plasticity of carboxysome building components in  
416 the cells grown under not only the same environmental condition but also a range of various  
417 conditions (Figure 6A). Our observations elucidate the size variation of  $\beta$ -carboxysomes in  
418 Syn7942 cells grown under distinct environmental conditions (Figure 6B) and adjustable  
419 carbon fixation capacities of carboxysomes that may be closely linked to the protein  
420 organization and size of carboxysomes. Variations in the diameter of intact carboxysomes,  
421 ranging from 90 to 600 nm, have been also shown in previous studies not only in single  
422 species but also among distinct species (Shively et al., 1973; Price and Badger, 1991; Iancu  
423 et al., 2007; Liberton et al., 2011), suggesting the adaptation strategies exploited by  
424 cyanobacteria for regulating their CO<sub>2</sub>-fixing machines to survive in diverse niches. It may be  
425 related to the environment-sensitive protein-protein interactions that drive protein self-  
426 assembly and BMC formation (Faulkner et al., 2019). Moreover, the spatial positioning and  
427 mobility of  $\beta$ -carboxysomes in live cells appear to be independent of carboxysome diameter

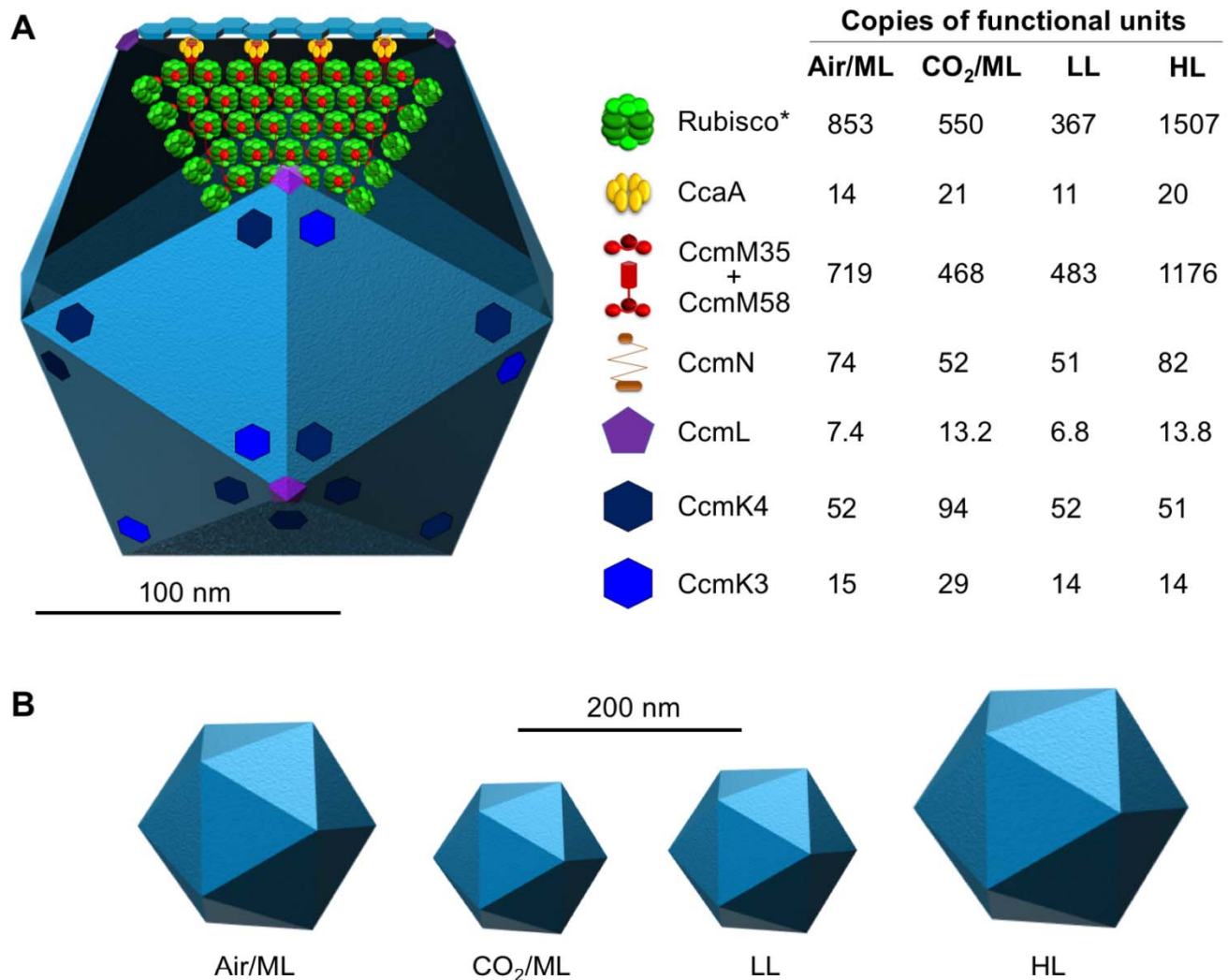


**Figure 6. Model of the  $\beta$ -carboxysome structure and protein stoichiometry.**

**(A)** Diagram of an icosahedral carboxysome structure and organization of building components. The stoichiometry of each building component within the carboxysome and its variations in response to changes in CO<sub>2</sub> and light intensity are shown on the right (See also Table 1). \*Rubisco content was estimated from RbcS stoichiometry based on the RbcL<sub>8</sub>S<sub>8</sub> Rubisco structure. The majority of shell facets shown in light blue is tiled by the major shell protein CcmK2. The total abundance of CcmM58 and CcmM35 was estimated. The components RbcL, CcmK2, CcmO and CcmP were not directly determined in this work and thus are not shown in this model.

**(B)** The carboxysome diameter is variable in response to changes in the CO<sub>2</sub> level and light intensity.

428 but show a strong dependence to light intensity, suggesting that light-dependent mechanisms  
 429 might mediate carboxysome location and diffusion. Carboxysome spacing and partitioning  
 430 have been suggested to be driven by different possible mechanisms, such as the cytoskeletal  
 431 proteins ParA and MreB (Savage et al., 2010), ParA-mediated chromosome segregation (Jain

432 et al., 2012) via filament-pull model (Ringgaard et al., 2009) or a diffusion-ratchet model  
433 (Vecchiarelli et al., 2013) as well as very recently the McdA and McdB that utilize a Brownian-  
434 ratchet mechanism to position carboxysomes (MacCready et al., 2018). Altogether, the  
435 organizational flexibility of  $\beta$ -carboxysomes, including modulatable protein stoichiometry,  
436 diameter and mobility, may represent the natural strategies for modifying shell permeability  
437 and enzyme encapsulation and ensuring structural and functional adaptations dependent on  
438 the local cellular environment.

439  
440 The estimated number of CcmL pentamers per carboxysome could be less than 12,  
441 demonstrating explicitly that it is not a prerequisite for CcmL pentamers to occupy all 12  
442 vertices of the icosahedral shell to ensure complete formation of functional carboxysomes.  
443 This hypothesis has been validated by previous observations that BMC shells in the absence  
444 of pentamers have no significant morphological changes (Cai et al., 2009; Lassila et al., 2014;  
445 Hagen et al., 2018a). These “non-complete capped” forms appear to be prevalent among the  
446 resultant carboxysomes under Air/ML and LL (Figure 2C), unlike the procarboxysomes  
447 (Cameron et al., 2013) or “immature” carboxysomes which are incapable of establishing an  
448 oxidative microenvironment for cargo enzymes (Chen et al., 2013). Whether the loss of  
449 capping CcmL will create large space within the shell, as a possible mechanism of modulating  
450 shell permeability, or will be compensated for by incorporation of other shell proteins, for  
451 example the additional CcmP trimers that are speculated to be responsible for permeability,  
452 remains to be further investigated. Our results also suggest that carboxysomes could possess  
453 a flexible molecular architecture, resonating with the observation of structural “breathing” of  
454 virus capsids which has been reported to be key to cope with temperature change (Roivainen  
455 et al., 1993; Li et al., 1994). Carboxysomes, though structurally resembling virus capsids,  
456 have been shown to be mechanically softer than the P22 virus capsid by a factor of  $\sim 10$ ,  
457 suggesting greater flexibility of protein-protein interactions within the carboxysome structure  
458 (Faulkner et al., 2017). The capping flexibility of pentamers may represent the dynamic nature  
459 of shell assembly probably in the second timescale and tunable protein-protein interactions in  
460 the shell, as characterized recently (Sutter et al., 2016; Faulkner et al., 2019).

461  
462 It was proposed that CcmM58 proteins are confined to a subshell layer for linking Rubisco,  
463 CcaA and CcmN to the shell, whereas CcmM35 molecules are predominantly located in the  
464 core to stimulate Rubisco aggregation (Rae et al., 2013). A recent study revealed that

465 CcmM35 and CcmM58 display similar distribution profiles in carboxysomes and are both  
466 integrated within the core of the carboxysome (Niederhuber et al., 2017). Fluorescence  
467 tagging at the protein C-terminus exploited in this work allowed us to only estimate the total  
468 amounts of CcmM but not distinguish CcmM35 and CcmM58, which can be addressed by N-  
469 terminal labeling of CcmM58 in our future study. Compared with the previous model that was  
470 based on protein stoichiometry of cell lysates (Long et al., 2011), our relative quantifications  
471 determined under the Air/ML condition show the 4.9-fold and 2.2-fold increases in the ratios of  
472 Rubisco/CcmM and Rubisco/CcaA, respectively (Figure 6A, Supplemental Table 5). The  
473 discrepancy may be caused by different sampling methods and cultivation conditions.

474  
475 Based on immunoblot analysis of cell lysates, the previous model has proposed an  
476 imbalanced ratio of RbcL to RbcS (~8:5), likely due to the binding of CcmM to Rubisco  
477 replacing 3 RbcS subunits (Long et al., 2011). This result was similar to our immunoblot  
478 quantification from cell lysates (Supplemental Table 2). Recent studies indicate that CcmM  
479 interacts with Rubisco (RbcL<sub>8</sub>S<sub>8</sub>) at distinct sites, without displacing RbcS (Ryan et al., 2018;  
480 Wang et al., 2019). Based on the L<sub>8</sub>S<sub>8</sub> ratio and RbcS abundance per carboxysome  
481 determined, we estimate that there are approximately 853, 550, 367, and 1507 copies of  
482 Rubisco per  $\beta$ -carboxysome under Air/ML, CO<sub>2</sub>/ML, LL, and HL, respectively (Figure 6A,  
483 Table 1). Even the lowest Rubisco abundance per  $\beta$ -carboxysome (an average diameter of  
484 151 nm) under LL is still greater than the Rubisco abundance per  $\alpha$ -carboxysome (an average  
485 diameter of 123 nm) (Iancu et al., 2007) by a factor of 1.6. This finding confirms the different  
486 interior organization of the two classes of carboxysomes: densely packed with Rubisco  
487 forming paracrystalline arrays inside the  $\beta$ -carboxysome (Faulkner et al., 2017) and random  
488 packing of Rubisco in the  $\alpha$ -carboxysome (Iancu et al., 2007; Iancu et al., 2010). The different  
489 interior structures may be ascribed to their distinct biogenesis pathways: biogenesis of  $\beta$ -  
490 carboxysomes is initiated from the nucleation of Rubisco and CcmM35 and then the shell  
491 encapsulation (Cameron et al., 2013); whereas  $\alpha$ -carboxysome assembly appears to start  
492 from shell formation (Menon et al., 2008) or a simultaneous shell-interior assembly (Iancu et  
493 al., 2010).

494  
495 While the abundance of most of the structural components varies, the ratio of CcmK4 and  
496 CcmK3 is relatively unaffected (ranging from 3.6 to 4.1, Supplemental Table 5) under the  
497 tested growth conditions, implying their spatial colocalization within the carboxysome shell

498 (Figure 6A). This is reminiscent of the recent observation that CcmK3 and CcmK4 can form a  
499 heterohexameric complex with a 1:2 stoichiometry and further form dodecamers in a pH-  
500 dependent manner (Sommer et al., 2019). The *ccmK3* and *ccmK4* genes are located in the  
501 same operon that is distant from the *ccm* operon and they may have different expression  
502 regulation compared with other carboxysome components (Rae et al., 2012; Sommer et al.,  
503 2017). The balanced expression and structural cooperation of CcmK3 and CcmK4 may be  
504 crucial for the fine-tuning of carboxysome permeability towards environmental stress.

505

506 Rational design, construction and modulation of bioinspired materials with structural and  
507 functional integrity are the major challenges in synthetic biology and protein engineering.  
508 Given their self-assembly, modularity and high efficiency in enhancing carbon fixation,  
509 carboxysomes have attracted tremendous interest to engineering this CO<sub>2</sub>-fixing organelle  
510 into other organisms, for example C<sub>3</sub> plants, with the intent of increasing photosynthetic  
511 efficiency and crop production (Lin et al., 2014b; Lin et al., 2014a; Occhialini et al., 2016;  
512 Long et al., 2018). Recently, we have reported the engineering of functional β-carboxysome  
513 structures in *E. coli* – a step towards constructing functional β-carboxysomes in eukaryotic  
514 organisms (Fang et al., 2018). Our present study, by evaluating the actual protein  
515 stoichiometry and structural variability of native β-carboxysomes, sheds light on the molecular  
516 basis underlying the assembly, formation and regulation of functional carboxysomes. It will  
517 empower bioengineering to construct BMC-based nano-bioreactors and scaffolds, with  
518 functional and tunable compositions and architectures, for metabolic reprogramming and  
519 targeted synthetic molecular delivery. A deeper understanding of carboxysome structure and  
520 the developed imaging techniques will be broadly extended to other BMCs and  
521 macromolecular systems.

522

523

## 524 **Materials and Methods**

### 525 **Bacterial strains, growth conditions, light and CO<sub>2</sub> treatment, and generation of** 526 **mutants**

527 Wild-type (WT) and mutant *Synechococcus elongatus* PCC7942 (Syn7942) strains were  
528 grown in BG-11 medium in culture flasks with constant shaking or on BG-11 plates containing  
529 1.5% (w/v) agar at 30°C. Syn7942 WT and mutants were maintained and grown under  
530 different intensities of constant white LED light illumination: 80 μE·m<sup>-2</sup>·s<sup>-1</sup> as HL (higher light

531 in ambient air),  $50 \mu\text{E}\cdot\text{m}^{-2}\cdot\text{s}^{-1}$  as Air/ML (moderate light in ambient air),  $10 \mu\text{E}\cdot\text{m}^{-2}\cdot\text{s}^{-1}$  as LL  
532 (lower light in ambient air) to ensure full acclimation, respectively. Cultures were grown in air  
533 without an additional  $\text{CO}_2$  source, except for the  $\text{CO}_2$  treatment experiment in which Syn7942  
534 cultures in the growth incubators were aerated with 3%  $\text{CO}_2$  under moderate light ( $\text{CO}_2/\text{ML}$ ).

535

536 Cultures were constantly diluted with fresh medium to maintain exponential growth phase for  
537 the following imaging and biochemical analysis. *Escherichia coli* strains used in this work,  
538 DH5a and BW25113, were grown aerobically at 30 or 37°C in Luria-Broth medium. Medium  
539 supplements were used, where appropriate, at the following final concentrations: ampicillin  
540  $100 \text{ mg}\cdot\text{mL}^{-1}$ , chloramphenicol  $10 \text{ mg}\cdot\text{mL}^{-1}$ , apramycin  $50 \text{ mg}\cdot\text{mL}^{-1}$ , and arabinose 100 mM.

541

542 All YFP-fusion mutants were generated following the REDIRECT protocol (Supplemental  
543 Figure 1) (Gust et al., 2002), by inserting the *eyfp:apramycin* DNA fragment to the C-terminus  
544 of individual carboxysome genes based on homologous recombination (Supplemental Table  
545 6). Primers used in this work were listed in Supplemental Table 7. The same strategy was  
546 also applied for the mYPet mutant. For these mutant strains, BG-11 medium was  
547 supplemented with apramycin at  $50 \mu\text{g}\cdot\text{mL}^{-1}$ .

548

#### 549 **Cell doubling time and growth curve measurement**

550 Cultures were inoculated at  $\text{OD}_{750}$  of 0.05-0.1 with fresh BG-11. Growth of cells was  
551 monitored at  $\text{OD}_{750}$  using a spectrophotometer (Jenway 6300 spectrophotometer, Jenway,  
552 UK) every 24 hours. Doubling times were calculated using exponential phase of growth from  
553 day 1 to day 4. Four biological replicates from different culture flasks were recorded. Data are  
554 presented as mean  $\pm$  standard deviation (SD). For each experiment, at least three biological  
555 replicates from different culture flasks were analyzed.

556

#### 557 **Slimfield microscopy and data analysis**

558 Live cells were applied at the small volume onto the BG-11 agarose pad at 0.25 mm  
559 thickness to maintain physiological growth, air dried to remove excessive medium and then  
560 assembled with plasma cleaned (Harrick-Plasma) glass cover slips. A dual-color bespoke  
561 laser excitation single-molecule fluorescence microscope was used utilizing narrow  
562 epifluorescence excitation of 10  $\mu\text{m}$  full width at half maximum (FWHM) in the sample plane



563 to generate Slimfield illumination using narrowfield epifluorescence (Wollman and Leake,  
564 2016; Wollman et al., 2016b; Wollman et al., 2017). This was incident on a sample mounted  
565 on a Mad City Labs nanostage built on an inverted Zeiss microscope body consisting of a 20  
566 mW 514 nm wavelength laser. A Chroma GFP/mCherry dichroic was mounted under the  
567 Olympus 100x NA = 1.49 TIRF (total internal reflection fluorescence) objective, which delivers  
568 10 mW excitation power. The image was split into YFP and chlorophyll channels using a  
569 bespoke color splitter utilizing a Chroma dichroic split at 560 nm with 542 nm and 600 nm, 25  
570 nm bandwidth filters. Imaging was done with an Andor iXon 128 x 128 pixel EMCCD camera  
571 (iXon DV860-BI, Andor Technology, UK), at a pixel magnification of 80 nm/pixel using 5 ms  
572 camera exposure time. Excitation intensity was initially reduced by 100x using and ND = 2 or  
573 1 attenuation filter for high copy number strains (all except CcmL and RbcX) to avoid pixel  
574 saturation on the EMCCD camera detector before a full-power photobleaching. Sample sizes  
575 for individual strains are 60 (RbcS), 219 (CcmK3), 77 (CcmK4), 316 (CcmL), 71 (CcmM), 86  
576 (CcmN), 95 (CcaA) and 211 (RbcX), respectively. Each population of carboxysomes comes  
577 from 20-30 fields of view, with 1-7 cells per field of view.

578

579 The analysis was performed using bespoke MATLAB (Mathworks) software (Miller et al.,  
580 2015) with previously outlined methods (Llorente-Garcia et al., 2014; Wollman et al., 2016a;  
581 Beattie et al., 2017; Lund et al., 2018; Stracy et al., 2018). In brief, candidate bright  
582 fluorescent foci were identified in images using morphological transformation and thresholding.  
583 The sub-pixel centroids of these foci were determined using iterative Gaussian masking and  
584 their intensity quantified as the summed intensity inside a 5-pixel radius region of interest  
585 (ROI) corrected for the mean background intensity inside a surrounding 17 x 17 pixel ROI  
586 (Delalez et al., 2010; Leake, 2014). Foci were accepted and tracked through time if they had  
587 a signal-to-noise ratio, defined as the mean intensity in the circular ROI divided by the  
588 standard deviation in the outer ROI, over 0.4. The characteristic intensity of single  
589 YFP/mYPet was measured from the distribution of detected foci intensity towards the end of  
590 the photobleaching (Figure 1), confirmed by comparing the obtained value to individual  
591 photobleaching steps obtained using edge-preserving filtration (Figure 1) (Leake et al., 2003;  
592 Leake et al., 2004). The stoichiometry of foci was then determined through cell-by-cell based  
593 Slimfield imaging using numerical integration of pixel intensities (Wollman and Leake, 2015)  
594 in each carboxysome divided by the intensity of a single YFP (Figure 1B).

595

596 For high-copy-number strains, intensity of carboxysomes was very high compared to the  
597 chlorophyll but for CcmL (typically ~2x, compare Supplemental Figure 3 with Supplemental  
598 Figure 4A) the fluorescence intensity per carboxysome was comparable (although generally  
599 brighter) to small regions of bright chlorophyll, detected as foci by our software, as confirmed  
600 by looking at the parental strain with no YFP present. To correct for this chlorophyll content,  
601 we tracked parental WT Syn7942 cells as YFP-labelled cells to calculate the apparent  
602 chlorophyll stoichiometry distribution (Supplemental Figure 4A). The CcmL distribution was  
603 then corrected by subtracting the apparent chlorophyll distribution. To investigate putative  
604 periodic features in the stoichiometry distribution, we used the raw uncorrected values to  
605 minimize dephasing artefacts (Figure 4C) using a kernel width of 0.5 molecules (equivalent to  
606 the error in determining the characteristic intensity). The peak values in other strains were far  
607 from the chlorophyll peak and so unaffected by this correction.

608

### 609 **Confocal microscopy imaging and data analysis**

610 Preparation of Syn7942 cells for confocal microscopy was performed as described earlier (Liu  
611 et al., 2012; Casella et al., 2017). Cells were maintained under different growth conditions  
612 prior to microscopy imaging, to ensure full acclimation. Confocal fluorescence images (12-bit,  
613 512 x 512 pixels) were recorded using a Zeiss LSM780 with an alpha Plan-Fluor 100x oil  
614 immersion objective (NA 1.45) and excitation at 514 nm from an Argon laser. YFP and  
615 chlorophyll fluorescence were captured at 520–550 nm and 660–700 nm, respectively. The  
616 image pixel size was 41.5 nm. The pixel dwell time was 0.64  $\mu$ s and the frame averaging was  
617 8, resulting in an effective frame time of ~1.5 s. The pinhole was set to give z axis resolution  
618 of 1  $\mu$ m. Live-cell confocal fluorescence images were recorded from at least five different  
619 cultures. The sample stage was pre-incubated and thermo-controlled at 30°C before and  
620 during imaging. Zoom settings were set to have each carboxysome visualized with a  
621 minimum of 8 x 8 pixels array to allow sufficient profiling of carboxysome signals by peak  
622 intensity recognition and measurement. All images were captured with all pixels below  
623 saturation.

624

625 Confocal microscopic images were processed using FIJI Trackmate plugins (Tinevez et al.,  
626 2017) to retrieve peak intensities of carboxysomes based on the Find Maxima detection  
627 algorithm. Noise tolerance was determined by background intensities in empty regions.  
628 Imaging for different treatments in the same strain was performed under the same imaging

629 settings. For strains with visible cytosolic signals, the cytosolic background intensity was  
630 determined by the average peak intensities in non-carboxysome regions over the central line  
631 of the cell and was subtracted to obtain peak intensities. Raw data were processed by Origin  
632 Lab and MATLAB (Mathworks) for profile extraction and statistical analysis and the goodness-  
633 of-fit parameter for Violin plot visualization. Violin plots were generated by R to illustrate the  
634 fluorescence intensity distribution of individual building proteins per carboxysome fitted by  
635 kernel smooth fitting. The representative values and deviations of signal intensities were  
636 represented by Peak value  $\pm$  half width at half maximum (HWHM) measured from kernel  
637 density fitted profiles, respectively. The significance of differences between treatments was  
638 evaluated by Mann-Whitney U-tests pair-wisely (Supplemental Table 4). Standard errors of  
639 sampling were determined through randomized grouping of intensity entries, with each group  
640 containing a minimum of 70–100 entries. Errors were controlled below 5% to have accurate  
641 estimation from the distributions. The relative protein abundance of carboxysomes was  
642 estimated by confocal imaging under Air/ML, CO<sub>2</sub>/ML, LL, and HL was normalized by the  
643 definite copy number of each strain under Air/ML determined by Slimfield imaging.

644

#### 645 **Live-cell time-lapse confocal imaging and data analysis**

646 A 2 mm-thick BG-11 agar mat was prepared in stacked sandwiches to accommodate drops of  
647 diluted Syn7942 cells. Cells were incubated on the BG-11 agar mat on the microscope for 1-2  
648 hours before imaging. The continuous light illumination was provided at the intensity relatively  
649 equal to HL, ML, or LL that were used for cell growth, in order to maintain cell physiology. The  
650 same illumination was applied to the cells during time-lapse imaging with a hand-made  
651 module that switched off the light during laser scanning (less than 5 s per minute intervals).  
652 The interval time was set to 60 s to guarantee sufficient light illumination between imaging.  
653 The laser power was set to the minimum (1%) to reduce the bleaching for signals during long-  
654 term tracking. Images were initially corrected for horizontal drifting by Descriptor-based series  
655 registration (2d/3d+T) plugin, and then were processed by the Trackmate plugin in FIJI for  
656 particle tracking. Retrieved track data was analyzed using bespoke MATLAB (Mathworks)  
657 scripts for MSD. Diffusion coefficient calculations and data visualization were modified as  
658 previously described (Ewers et al., 2005; Sbalzarini and Koumoutsakos, 2005). Diffusion  
659 coefficients were calculated by fitting the first 6 points of the MSD vs.  $\tau$  curves. As the MSD  
660 vs.  $\tau$  curves indicated potentially non-Brownian diffusion at higher  $\tau$  values, we described the  
661 diffusion coefficients as “apparent diffusion coefficients”. Tracking and diffusion coefficient

662 determination were tested by computational simulations (Supplemental Movie 2). Bespoke  
663 Matlab code was written to generate simulated image stacks of carboxysomes diffusing inside  
664 cells. Images were simulated by integrating a model 3D point spread function over a 3D  
665 model for the cell structure (Wollman and Leake 2015). This model comprises an inner  
666 cytosol surrounded by thylakoid membranes (indicated by chlorophyll fluorescence) and 3  
667 carboxysomes with a diameter of 200 nm. Each component's intensity was adjusted to match  
668 real images before representative Poisson noise was applied. Carboxysomes were simulated  
669 undergoing Brownian motion with a diffusion coefficient of  $1.3 \times 10^{-5} \mu\text{m}^2 \cdot \text{s}^{-1}$  over 40 image  
670 frames. Trackmate tracking and diffusion coefficient calculation yielded a mean diffusion  
671 coefficient of  $1.32 \pm 0.02 \times 10^{-5} \mu\text{m}^2 \cdot \text{s}^{-1}$ , giving a 1.5% error.

672

### 673 **Immunoblot analysis**

674 Immunoblot examination was carried out following the procedure described previously (Sun et  
675 al., 2016). 150  $\mu\text{g}$  of cell lysate, measured by Pierce Coomassie (Bradford) Protein Assay Kit  
676 (Thermo Fisher Scientific), was loaded on 10% (v/v) denaturing SDS-PAGE gels. Immunoblot  
677 analysis was performed using the primary mouse monoclonal anti-GFP (Invitrogen, 33-2600),  
678 capable of recognizing series of GFP variants including YFP, the rabbit polyclonal anti-RbcL  
679 (Agrisera, AS03 037), the horseradish peroxidase-conjugated goat anti-mouse IgG secondary  
680 antibody (Promega, W4021) and a Goat anti-Rabbit IgG (H&L), HRP conjugated (Agrisera  
681 AS10 1461). Anti-CcmK2 antibody was kindly provided by the Kerfeld lab (Michigan State  
682 University, US) (Cai et al., 2016). Protein quantification from immunoblot data was carried out  
683 using FIJI. Our nominal assumption that the ratios of YFP-tagged to total RbcL or CcmK2 in  
684 carboxysomes are similar to those in cell lysates.

685

### 686 ***In vivo* carbon fixation assay**

687 *In vivo* carbon fixation assay was carried out to determine carbon fixation of Syn7942 WT and  
688 mutant cells, as described in the previous work (Sun et al., 2016). For each WT and mutant,  
689 at least three biological replicates from different culture flasks were assayed. Significance was  
690 assessed by two-tailed Student's t-tests.

691

### 692 **Electron microscopy and carboxysome size measurement**

693 Electron microscopy was carried out as described previously (Liu et al., 2008; Sun et al.,  
694 2016). Carboxysome diameter was measured as described previously (Faulkner et al., 2017)  
695 and was analyzed using Origin.

696

## 697 **Accession Numbers**

698 Accession numbers of genes in this article are provided in Supplemental Table 6.

699

## 700 **Supplemental Data**

701 **Supplemental Figure 1.** Construction and verification of Syn7942 strains with YFP fusion to  
702 individual carboxysome proteins.

703 **Supplemental Figure 2.** Immunoblot analysis of the YFP-tagged Syn7942 strains using the  
704 anti-GFP, anti-RbcL and anti-CcmK antibodies of soluble fractions in this study based on  
705 SDS-PAGE.

706 **Supplemental Figure 3.** Slimfield images of YFP-fusion cells under Air/ML and stoichiometric  
707 histogram of copies of YFP molecules per carboxysome.

708 **Supplemental Figure 4.** Normalization of chlorophyll during Slimfield imaging for Syn7942  
709 strains.

710 **Supplemental Figure 5.** Comparison of YFP and mYPet tagging to RbcL reveals no  
711 differences in carboxysome localization, cell growth and carbon fixation, suggesting that there  
712 are no measurable artefacts due to putative effects of dimerization of the YFP tag.

713 **Supplemental Figure 6.** Confocal images of YFP-tagged cells.

714 **Supplemental Figure 7.** Confocal images of RbcS-YFP, CcmM-YFP, CcmK4-YFP and  
715 CcmK3-YFP cells under Air/ML, CO<sub>2</sub>, LL, and HL and distribution profiles of carboxysome  
716 protein signal intensity.

717 **Supplemental Figure 8.** Confocal images of CcmL-YFP, CcmN-YFP, CcaA-YFP and RbcX-  
718 YFP cells under Air/ML, CO<sub>2</sub>, LL, and HL and distribution profiles of carboxysome protein  
719 signal intensity (continuing Supplemental Figure 7).

720 **Supplemental Figure 9.** Thin-section EM images of WT Syn7942 cells under Air/ML, CO<sub>2</sub>/ML,  
721 LL and HL.

722 **Supplemental Figure 10.** Changes in the diffusion coefficient of carboxysomes in Syn7942  
723 cells under HL, ML and LL are not dependent on the carboxysome size.

724 **Supplemental Figure 11.** CcmP-YFP and CcmO-YFP Syn7942 cells.

725 **Supplemental Table 1.** Cell growth, carbon fixation and cell dimensions of Syn7942 WT and  
726 YFP-fusion mutants under Air/ML.

727 **Supplemental Table 2.** Immunoblotting estimation of the stoichiometry of carboxysomal  
728 proteins in cell lysates.

729 **Supplemental Table 3.** Carboxysome content per cell under Air/ML, CO<sub>2</sub>/ML, LL and HL  
730 determined by confocal imaging.

731 **Supplemental Table 4.** Evaluation and quality control of quantitative microscopy.

732 **Supplemental Table 5.** Carboxysome properties in Syn7942 vary under Air/ML, CO<sub>2</sub>/ML, LL  
733 and HL, determined by Slimfield, confocal and EM imaging.

734 **Supplemental Table 6.** Accession numbers for genes/proteins in this work.

735 **Supplemental Table 7.** PCR primers used in this study for gene cloning and sequencing.

736 **Supplemental Movie 1.** Time-lapse confocal imaging reveals different diffusion dynamics of  
737 carboxysomes in the RbcL-YFP Syn7942 cells grown under HL, ML and LL conditions.

738 **Supplemental Movie 2.** Simulations of diffusing carboxysomes *in cellulo* validate tracking  
739 and diffusion coefficient determination.

740

## 741 **Acknowledgements**

742 We thank Gregory F Dykes, Selene Casella and Alison Beckett for technical support of  
743 electron microscopy. We thank David Mason in confocal image analysis. We thank the  
744 Liverpool Centre for Cell Imaging for technical assistance and provision. Y.S., F.H. and L.-N.L.  
745 were supported by Royal Society (UF120411, IE131399, RGF\EA\180233, RGF\EA\181061  
746 and URF\R\180030, L.-N.L.) and Biotechnology and Biological Sciences Research Council  
747 Grant (BB/M024202/1 and BB/R003890/1, L.-N.L.), Leverhulme Trust (ECF-2016-778, F.H.)  
748 and China Scholarship Council (Y.S.). M.L. was supported by a Medical Research Council  
749 grant (MR/K01580X/1), Biotechnology and Biological Sciences Research Council Grant  
750 (BB/N006453/1). A.J.M.W. was part-funded by the Wellcome Trust (204829) through Centre  
751 for Future Health at the University of York.

752

753

## 754 **Author contributions**

755 L.-N.L and M.C.L designed research; Y.Q. A.J.M.W and F.H. performed research and  
756 analyzed data; L.-N.L, Y.Q., M.C.L., and A.J.M.W. wrote the paper.

757

758

## 759 **Competing interests**

760 The authors declare no conflict of interest.

761

762

## 763 **Figure legends**

### 764 **Figure 1. Slimfield quantification of cells grown under ambient air/moderate light** 765 **Air/ML conditions.**

766 **(A)** Averaged Slimfield images of YFP fluorescence (green) over 5 frames of strains  
767 expressing shell component CcmK4-YFP, the interior enzyme RbcS-YFP, and the shell-  
768 interior linker protein CcmM-YFP. White dashed lines indicate cell body outlines.

769 **(B)** Distribution of the intensities of automatically detected foci from the end of  
770 photobleaching, corresponding to the characteristic intensity of *in vivo* YFP. Inset shows the  
771 Fourier spectrum of ‘overtracked’ foci, tracked beyond photobleaching, showing a peak at the  
772 characteristic intensity.

773 **(C)** Representative fluorescence photobleaching tracked at ultra-fast speed. The CcmK4 plot  
774 shows an inset ‘zoomed in’ on lower intensity range with step-preserving Chung-Kennedy  
775 filtered data in red, showing individual photobleaching steps clearly visible at the  
776 characteristic intensity. Brightness (kcounts), counts measured per camera pixel multiplied by  
777 1,000.

778 **(D)** Distribution of YFP copy number detected for individual carboxysomes in corresponding  
779 mutants, rendered as kernel density estimates using standard kernel width. Heterogeneity of  
780 contents was observed, and a “preferable” copy number, represented by kernel density peak  
781 values could be determined. Statistics of copy numbers (Peak value  $\pm$  HWHM) are listed in  
782 Table 1 for ML conditions. The corresponding Slimfield images and histogram for complete  
783 strain sets are shown in Supplemental Figure 3.

784

### 785 **Figure 2. Relative protein quantification of CcmK4, RbcS and CcmM in the** 786 **carboxysome under different CO<sub>2</sub> levels and light intensities using confocal** 787 **microscopy.**

788 **(A)** Confocal images of CcmK4-YFP, RbcS-YFP and CcmM-YFP strains under Air/ML,  
789 CO<sub>2</sub>/ML, LL and HL. Fluorescence foci (green) indicate carboxysomes, and cell borders were  
790 outlined by white dashed lines. Scale bar indicates 2  $\mu$ m.

791 **(B)** Violin plot of carboxysome intensities under Air/ML, CO<sub>2</sub>/ML, LL and HL, normalized to  
792 kernel density ML peak values (peaks marked by white dashed lines).

793 **(C)** Kernel density estimates of CcmL carboxysome copy number grown under Air/ML, CO<sub>2</sub>,  
794 LL and HL detected by Slimfield and corrected for chlorophyll. Triple Gaussian fits are  
795 indicated as colored dashed lines with the summed fit in red. The percentage in each  
796 Gaussian is indicated aside.

797

### 798 **Figure 3. Changes in carboxysome protein stoichiometry upon increases in CO<sub>2</sub> levels** 799 **and light intensity.**

800 **(A)** Comparison of carboxysome protein stoichiometry under CO<sub>2</sub> treatment. Increase in the  
801 CO<sub>2</sub> concentration resulted in the rise of CcmK3, CcmK4, CcaA and CcmL contents and the  
802 decline of RbcS, CcmN and CcmM contents.

803 **(B)** Comparison of carboxysome protein stoichiometry under light intensity treatment.  
804 Increased light intensity led to the elevation of RbcS, CcmM, CcmL, CcaA and CcmN  
805 contents, whereas the abundance of RbcX, CcmK3 and CcmK4 contents per carboxysome  
806 did not change dramatically.  
807 Mann-Whitney U-tests were performed to compare the numbers of functional units of  
808 individual carboxysome proteins changed from CO<sub>2</sub>/ML to Air/ML (A) and from HL to LL (B). \*,  
809  $p < 0.05$ ; \*\*\*,  $p < 0.005$ ; *ns*,  $p > 0.05$ .  
810

811 **Figure 4. Variations of the carboxysome size and carbon fixation under Air/ML, CO<sub>2</sub>, LL**  
812 **and HL.**

813 **(A)** Thin-section electron microscopy (EM) images showing individual carboxysomes in the  
814 Syn7942 WT cells under Air/ML, CO<sub>2</sub>, LL and HL treatments Yellow arrows indicate the  
815 carboxysomes with spaces of low protein density under LL. More EM images are shown in  
816 Supplemental Figure 9. Scale bar indicates 1  $\mu$ m.

817 **(B)** Changes in the carboxysome diameter under Air/ML, CO<sub>2</sub>, LL and HL measured from EM  
818 ( $n = 33, 25, 27$  and  $51$ , respectively), with representative carboxysome images depicted  
819 above. Dashed lines indicate medians and solid lines indicate means. Differences in the  
820 carboxysome diameter are significant between CO<sub>2</sub> and air ( $p = 1.92 \times 10^{-14}$ ) and between LL  
821 and HL ( $p = 8.29 \times 10^{-7}$ ), indicated as \*\*\*.

822 **(C)** Correlation between the carboxysome size and the Rubisco content per carboxysome  
823 under Air/ML, CO<sub>2</sub>, LL and HL.

824 **(D)** Correlation between the carboxysome size and CO<sub>2</sub> fixation per carboxysome.

825 **(E)** Correlation between the carboxysome size and CO<sub>2</sub> fixation per Rubisco of the  
826 carboxysomes. Carboxysome diameters and CO<sub>2</sub> fixation are presented as average  $\pm$  SD,  
827 whereas the carboxysome total protein content and Rubisco content are shown as Peak  
828 value  $\pm$  HWHM.  
829

830 **Figure 5. Spatial localization and diffusion dynamics of carboxysomes in Syn7942 cells**  
831 **are dependent on light intensity.**

832 **(A)** Tracking of carboxysome diffusion in cells grown under HL, ML and LL. Colored lines  
833 indicate the diffusion trajectories of each carboxysomes and circles represent the diffusion  
834 areas of each carboxysomes over 60 mins. Scale bar indicates 1  $\mu$ m.

835 **(B)** Non-linear MSD (Mean Square Displacement) vs. the time interval ( $\tau$ ) profiles suggest the  
836 mobility of carboxysomes in Syn7942 cells grown under HL, ML and LL. Inset, zoom-in view  
837 of the MSD profile under LL.

838 **(C)** Diffusion coefficient of carboxysomes *in vivo* decreases significantly when the light  
839 intensity reduces:  $2.76 \pm 2.83 \times 10^{-5} \mu\text{m}^2 \cdot \text{s}^{-1}$  for HL (mean  $\pm$  SD,  $n = 105$ ),  $1.48 \pm 1.03 \times 10^{-5}$   
840  $\mu\text{m}^2 \cdot \text{s}^{-1}$  for ML ( $n = 84$ ), and  $0.28 \pm 0.19 \times 10^{-5} \mu\text{m}^2 \cdot \text{s}^{-1}$  for LL ( $n = 336$ ).  $p = 3.05 \times 10^{-5}$   
841 between HL and ML;  $p = 2.77 \times 10^{-5}$  between ML and LL, two-tailed Student's t-test).  
842

843 **Figure 6. Model of the  $\beta$ -carboxysome structure and protein stoichiometry.**

844 **(A)** Diagram of an icosahedral carboxysome structure and organization of building  
845 components. The stoichiometry of each building component within the carboxysome and its  
846 variations in response to changes in CO<sub>2</sub> and light intensity are shown on the right (See also  
847 Table 1). \*Rubisco content was estimated from RbcS stoichiometry based on the RbcL<sub>8</sub>S<sub>8</sub>  
848 Rubisco structure. The majority of shell facets shown in light blue is tiled by the major shell



849 protein CcmK2. The total abundance of CcmM58 and CcmM35 was estimated. The  
850 components RbcL, CcmK2, CcmO and CcmP were not directly determined in this work and  
851 thus are not shown in this model.

852 **(B)** The carboxysome diameter is variable in response to changes in the CO<sub>2</sub> level and light  
853 intensity.

854

855 **Table 1.** Protein stoichiometry of the Syn7942  $\beta$ -carboxysome and its variability in cells grown under Air/ML, CO<sub>2</sub>/ML, LL and HL  
856 conditions determined from Slimfield and confocal microscopy. Stoichiometry is presented as Peak value  $\pm$  HWHM and the sample sizes  
857 are indicated as *n*. Peak values were determined from Slimfield stoichiometry profiles of each carboxysome proteins (Figure 1,  
858 Supplemental Figure 3). Quantification of CcmL under the four conditions was acquired from Slimfield for accurate measurement of  
859 copies of shell pentamers for capping the carboxysome structure. Copies of other carboxysome proteins were calculated using Slimfield  
860 results (bold) with definitive counts of protein copies under Air/ML (See also Supplemental Figure 3) in combination with relative  
861 quantification of each protein under the four conditions from confocal imaging (See also Supplemental Figure 7 and 8). Protein structures  
862 were derived from previous studies (Kerfeld et al., 2005; Long et al., 2007; Tanaka et al., 2007; Tanaka et al., 2008; Long et al., 2011;  
863 Kinney et al., 2012; McGurn et al., 2016). \*Monomeric unit of CcmM was designated to CcmM35 that is the majority of CcmM; CcmM58  
864 is postulated as a trimer.  
865

Category	Structure	Protein	Air/ML		CO <sub>2</sub> /ML		LL		HL	
			Peak value $\pm$ HWHM	Number of functional units	Peak value $\pm$ HWHM	Number of functional units	Peak value $\pm$ HWHM	Number of functional units	Peak value $\pm$ HWHM	Number of functional units
Shell proteins	Hexamer	CcmK3	<b>92 <math>\pm</math> 148</b> ( <i>n</i> = 219)	<b>15 <math>\pm</math> 25</b>	172 $\pm$ 83 ( <i>n</i> = 2048)	29 $\pm$ 14	83 $\pm$ 31 ( <i>n</i> = 1516)	14 $\pm$ 5	87 $\pm$ 52 ( <i>n</i> = 2155)	14 $\pm$ 9
		CcmK4	<b>314 <math>\pm</math> 194</b> ( <i>n</i> = 77)	<b>52 <math>\pm</math> 32</b>	562 $\pm$ 263 ( <i>n</i> = 1918)	94 $\pm$ 44	313 $\pm$ 121 ( <i>n</i> = 1766)	52 $\pm$ 20	304 $\pm$ 95 ( <i>n</i> = 3215)	51 $\pm$ 16
	Pentamer	CcmL	<b>37 <math>\pm</math> 17</b> ( <i>n</i> = 316)	<b>7.4 <math>\pm</math> 3.4</b>	<b>66 <math>\pm</math> 24</b> ( <i>n</i> = 311)	<b>13.2 <math>\pm</math> 4.8</b>	<b>34 <math>\pm</math> 15</b> ( <i>n</i> = 394)	<b>6.8 <math>\pm</math> 3.0</b>	<b>69 <math>\pm</math> 24</b> ( <i>n</i> = 220)	<b>13.8 <math>\pm</math> 4.8</b>
Structural proteins	Monomer*	CcmM	<b>719 <math>\pm</math> 1433</b> ( <i>n</i> = 71)	<b>719 <math>\pm</math> 1433</b>	468 $\pm$ 425 ( <i>n</i> = 2313)	468 $\pm$ 425	483 $\pm$ 366 ( <i>n</i> = 3655)	483 $\pm$ 366	1176 $\pm$ 691 ( <i>n</i> = 2318)	1176 $\pm$ 691
	Monomer	CcmN	<b>74 <math>\pm</math> 51</b> ( <i>n</i> = 86)	<b>74 <math>\pm</math> 51</b>	52 $\pm$ 28 ( <i>n</i> = 3143)	52 $\pm$ 28	51 $\pm$ 20 ( <i>n</i> = 4022)	51 $\pm$ 20	82 $\pm$ 34 ( <i>n</i> = 5074)	82 $\pm$ 34
CA	Hexamer	CcaA	<b>86 <math>\pm</math> 81</b> ( <i>n</i> = 95)	<b>14 <math>\pm</math> 14</b>	129 $\pm$ 86 ( <i>n</i> = 1354)	21 $\pm$ 14	65 $\pm$ 21 ( <i>n</i> = 217)	11 $\pm$ 4	122 $\pm$ 59 ( <i>n</i> = 2837)	20 $\pm$ 10
Rubisco enzyme	L <sub>8</sub> S <sub>8</sub>	RbcS	<b>6822 <math>\pm</math> 9200</b> ( <i>n</i> = 60)	<b>853 <math>\pm</math> 1150</b>	4401 $\pm$ 6655 ( <i>n</i> = 894)	550 $\pm$ 832	2934 $\pm$ 5492 ( <i>n</i> = 752)	367 $\pm$ 687	12057 $\pm$ 5186 ( <i>n</i> = 1974)	1507 $\pm$ 648
Rubisco chaperone	Dimer	RbcX	<b>39 <math>\pm</math> 32</b> ( <i>n</i> = 211)	<b>20 <math>\pm</math> 16</b>	38 $\pm$ 10 ( <i>n</i> = 1370)	19 $\pm$ 5	40 $\pm$ 9 ( <i>n</i> = 1402)	20 $\pm$ 5	40 $\pm$ 9 ( <i>n</i> = 1861)	20 $\pm$ 5

866

867

## Parsed Citations

**Axen, S.D., Erbilgin, O., and Kerfeld, C.A. (2014).** A taxonomy of bacterial microcompartment loci constructed by a novel scoring method. *PLoS Comput Biol* 10, e1003898.

Pubmed: [Author and Title](#)

Google Scholar: [Author Only Title Only Author and Title](#)

**Badrinarayanan, A, Reyes-Lamothe, R., Uphoff, S., Leake, M.C., and Sherratt, D.J. (2012).** In vivo architecture and action of bacterial structural maintenance of chromosome proteins. *Science* 338, 528-531.

Pubmed: [Author and Title](#)

Google Scholar: [Author Only Title Only Author and Title](#)

**Beattie, T.R., Kapadia, N., Nicolas, E., Uphoff, S., Wollman, A.J., Leake, M.C., and Reyes-Lamothe, R. (2017).** Frequent exchange of the DNA polymerase during bacterial chromosome replication. *eLife* 6, e21763.

Pubmed: [Author and Title](#)

Google Scholar: [Author Only Title Only Author and Title](#)

**Bobik, T.A., Lehman, B.P., and Yeates, T.O. (2015).** Bacterial microcompartments: widespread prokaryotic organelles for isolation and optimization of metabolic pathways. *Mol Microbiol* 98, 193-207.

Pubmed: [Author and Title](#)

Google Scholar: [Author Only Title Only Author and Title](#)

**Cai, F., Menon, B.B., Cannon, G.C., Curry, K.J., Shively, J.M., and Heinhorst, S. (2009).** The pentameric vertex proteins are necessary for the icosahedral carboxysome shell to function as a CO<sub>2</sub> leakage barrier. *PLoS One* 4, e7521.

Pubmed: [Author and Title](#)

Google Scholar: [Author Only Title Only Author and Title](#)

**Cai, F., Sutter, M., Cameron, J.C., Stanley, D.N., Kinney, J.N., and Kerfeld, C.A. (2013).** The structure of CcmP, a tandem bacterial microcompartment domain protein from the beta-carboxysome, forms a subcompartment within a microcompartment. *J Biol Chem* 288, 16055-16063.

Pubmed: [Author and Title](#)

Google Scholar: [Author Only Title Only Author and Title](#)

**Cai, F., Bernstein, S.L., Wilson, S.C., and Kerfeld, C.A. (2016).** Production and characterization of synthetic carboxysome shells with incorporated luminal proteins. *Plant Physiol* 170, 1868-1877.

Pubmed: [Author and Title](#)

Google Scholar: [Author Only Title Only Author and Title](#)

**Cameron, J.C., Wilson, S.C., Bernstein, S.L., and Kerfeld, C.A. (2013).** Biogenesis of a bacterial organelle: the carboxysome assembly pathway. *Cell* 155, 1131-1140.

Pubmed: [Author and Title](#)

Google Scholar: [Author Only Title Only Author and Title](#)

**Casella, S., Huang, F., Mason, D., ZHAO, G.Y., Johnson, G.N., Mullineaux, C.W., and Liu, L.N. (2017).** Dissecting the native architecture and dynamics of cyanobacterial photosynthetic machinery. *Mol Plant* 10, 1434-1448.

Pubmed: [Author and Title](#)

Google Scholar: [Author Only Title Only Author and Title](#)

**Chen, A.H., Robinson-Mosher, A., Savage, D.F., Silver, P.A., and Polka, J.K. (2013).** The bacterial carbon-fixing organelle is formed by shell envelopment of preassembled cargo. *PloS One* 8, e76127.

Pubmed: [Author and Title](#)

Google Scholar: [Author Only Title Only Author and Title](#)

**Dai, W., Chen, M., Myers, C., Ludtke, S.J., Montgomery Pettitt, B., King, J.A., Schmid, M.F., and Chiu, W. (2018).** Visualizing individual RuBisCO and its assembly into carboxysomes in marine cyanobacteria by cryo-electron tomography. *J Mol Biol*.

Pubmed: [Author and Title](#)

Google Scholar: [Author Only Title Only Author and Title](#)

**Delalez, N.J., Wadhams, G.H., Rosser, G., Xue, Q., Brown, M.T., Dobbie, I.M., Berry, R.M., Leake, M.C., and Armitage, J.P. (2010).** Signal-dependent turnover of the bacterial flagellar switch protein FliM. *Proc Natl Acad Sci U S A* 107, 11347-11351.

Pubmed: [Author and Title](#)

Google Scholar: [Author Only Title Only Author and Title](#)

**Dou, Z, Heinhorst, S., Williams, E.B., Murin, C.D., Shively, J.M., and Cannon, G.C. (2008).** CO<sub>2</sub> fixation kinetics of *Halothiobacillus neapolitanus* mutant carboxysomes lacking carbonic anhydrase suggest the shell acts as a diffusional barrier for CO<sub>2</sub>. *J Biol Chem* 283, 10377-10384.

Pubmed: [Author and Title](#)

Google Scholar: [Author Only Title Only Author and Title](#)

**Emlyn-Jones, D., Woodger, F.J., Price, G.D., and Whitney, S.M. (2006).** RbcX can function as a rubisco chaperonin, but is non-essential in *Synechococcus* PCC7942. *Plant Cell Physiol* 47, 1630-1640.

Pubmed: [Author and Title](#)

Google Scholar: [Author Only Title Only Author and Title](#)

Ewers, H., Smith, A.E., Sbalzarini, I.F., Lillie, H., Koumoutsakos, P., and Helenius, A (2005). Single-particle tracking of murine polyoma virus-like particles on live cells and artificial membranes. *Proc Natl Acad Sci U S A* 102, 15110-15115.

Pubmed: [Author and Title](#)

Google Scholar: [Author Only Title Only Author and Title](#)

Fang, Y., Huang, F., Faulkner, M., Jiang, Q., Dykes, G.F., Yang, M., and Liu, L.N. (2018). Engineering and modulating functional cyanobacterial CO<sub>2</sub>-fixing organelles. *Frontiers Plant Sci* 9, 739.

Pubmed: [Author and Title](#)

Google Scholar: [Author Only Title Only Author and Title](#)

Faulkner, M., Zhao, L.S., Barrett, S., and Liu, L.N. (2019). Self-assembly stability and variability of bacterial microcompartment shell proteins in response to the environmental change. *Nanoscale Research Letters* 14, 54.

Pubmed: [Author and Title](#)

Google Scholar: [Author Only Title Only Author and Title](#)

Faulkner, M., Rodriguez-Ramos, J., Dykes, G.F., Owen, S.V., Casella, S., Simpson, D.M., Beynon, R.J., and Liu, L.-N. (2017). Direct characterization of the native structure and mechanics of cyanobacterial carboxysomes. *Nanoscale* 9, 10662–10673.

Pubmed: [Author and Title](#)

Google Scholar: [Author Only Title Only Author and Title](#)

Gust, B., Kieser, T., and Chater, K.F. (2002). REDIRECT Technology: PCR-targeting System in *Streptomyces coelicolor*. (Norwich: John Innes Centre).

Pubmed: [Author and Title](#)

Google Scholar: [Author Only Title Only Author and Title](#)

Hagen, A., Sutter, M., Sloan, N., and Kerfeld, C.A. (2018a). Programmed loading and rapid purification of engineered bacterial microcompartment shells. *Nature Commun* 9, 2881.

Pubmed: [Author and Title](#)

Google Scholar: [Author Only Title Only Author and Title](#)

Hagen, A.R., Plegaria, J.S., Sloan, N., Ferlez, B., Aussignargues, C., Burton, R., and Kerfeld, C.A. (2018b). In vitro assembly of diverse bacterial microcompartment shell architectures. *Nano Lett* 18, 7030-7037.

Pubmed: [Author and Title](#)

Google Scholar: [Author Only Title Only Author and Title](#)

Harano, K., Ishida, H., Kittaka, R., Kojima, K., Inoue, N., Tsukamoto, M., Satoh, R., Himeno, M., Iwaki, T., and Wadano, A. (2003). Regulation of the expression of ribulose-1,5-bisphosphate carboxylase/oxygenase (EC 4.1.1.39) in a cyanobacterium, *Synechococcus PCC7942*. *Photosynth Res* 78, 59-65.

Pubmed: [Author and Title](#)

Google Scholar: [Author Only Title Only Author and Title](#)

Huang, F., Vasieva, O., Sun, Y., Faulkner, M., Dykes, G.F., Zhao, Z., and Liu, L.N. (2019). Roles of RbcX in carboxysome biosynthesis in the cyanobacterium *Synechococcus elongatus PCC7942*. *Plant Physiol* 179, 184-194.

Pubmed: [Author and Title](#)

Google Scholar: [Author Only Title Only Author and Title](#)

Iancu, C.V., Morris, D.M., Dou, Z., Heinhorst, S., Cannon, G.C., and Jensen, G.J. (2010). Organization, structure, and assembly of alpha-carboxysomes determined by electron cryotomography of intact cells. *J Mol Biol* 396, 105-117.

Pubmed: [Author and Title](#)

Google Scholar: [Author Only Title Only Author and Title](#)

Iancu, C.V., Ding, H.J., Morris, D.M., Dias, D.P., Gonzales, A.D., Martino, A., and Jensen, G.J. (2007). The structure of isolated *Synechococcus* strain WH8102 carboxysomes as revealed by electron cryotomography. *J Mol Biol* 372, 764-773.

Pubmed: [Author and Title](#)

Google Scholar: [Author Only Title Only Author and Title](#)

Jain, I.H., Vijayan, V., and O'Shea, E.K. (2012). Spatial ordering of chromosomes enhances the fidelity of chromosome partitioning in cyanobacteria. *Proc Natl Acad Sci U S A* 109, 13638-13643.

Pubmed: [Author and Title](#)

Google Scholar: [Author Only Title Only Author and Title](#)

Kerfeld, C.A., and Erbilgin, O. (2015). Bacterial microcompartments and the modular construction of microbial metabolism. *Trends Microbiol* 23, 22-34.

Pubmed: [Author and Title](#)

Google Scholar: [Author Only Title Only Author and Title](#)

Kerfeld, C.A., and Melnicki, M.R. (2016). Assembly, function and evolution of cyanobacterial carboxysomes. *Curr Opin Plant Biol* 31, 66-75.

Pubmed: [Author and Title](#)

Google Scholar: [Author Only Title Only Author and Title](#)

Kerfeld, C.A., Aussignargues, C., Zarzycki, J., Cai, F., and Sutter, M. (2018). Bacterial microcompartments. *Nat Rev Microbiol* 16, 277-290.

Pubmed: [Author and Title](#)

Google Scholar: [Author Only Title Only Author and Title](#)

Kerfeld, C.A., Sawaya, M.R., Tanaka, S., Nguyen, C.V., Phillips, M., Beeby, M., and Yeates, T.O. (2005). Protein structures forming the shell of primitive bacterial organelles. *Science* 309, 936-938.

Pubmed: [Author and Title](#)

Google Scholar: [Author Only Title Only Author and Title](#)

Kinney, J.N., Salmeen, A., Cai, F., and Kerfeld, C.A. (2012). Elucidating essential role of conserved carboxysomal protein CcmN reveals common feature of bacterial microcompartment assembly. *J Biol Chem* 287, 17729-17736.

Pubmed: [Author and Title](#)

Google Scholar: [Author Only Title Only Author and Title](#)

Larsson, A.M., Hasse, D., Vaeleard, K., and Andersson, I. (2017). Crystal structures of  $\beta$ -carboxysome shell protein CcmP: ligand binding correlates with the closed or open central pore. *J Exp Bot* 68, 3857-3867.

Pubmed: [Author and Title](#)

Google Scholar: [Author Only Title Only Author and Title](#)

Lassila, J.K., Bernstein, S.L., Kinney, J.N., Axen, S.D., and Kerfeld, C.A. (2014). Assembly of robust bacterial microcompartment shells using building blocks from an organelle of unknown function. *J Mol Biol* 426, 2217-2228.

Pubmed: [Author and Title](#)

Google Scholar: [Author Only Title Only Author and Title](#)

Leake, M.C. (2014). Analytical tools for single-molecule fluorescence imaging in cellulose. *Physical Chemistry Chemical Physics* 16, 12635-12647.

Pubmed: [Author and Title](#)

Google Scholar: [Author Only Title Only Author and Title](#)

Leake, M.C. (2018). Transcription factors in eukaryotic cells can functionally regulate gene expression by acting in oligomeric assemblies formed from an intrinsically disordered protein phase transition enabled by molecular crowding. *Transcription* 9, 298-306.

Pubmed: [Author and Title](#)

Google Scholar: [Author Only Title Only Author and Title](#)

Leake, M.C., Wilson, D., Bullard, B., and Simmons, R.M. (2003). The elasticity of single kettin molecules using a two-bead laser-tweezers assay. *FEBS Lett* 535, 55-60.

Pubmed: [Author and Title](#)

Google Scholar: [Author Only Title Only Author and Title](#)

Leake, M.C., Wilson, D., Gautel, M., and Simmons, R.M. (2004). The elasticity of single titin molecules using a two-bead optical tweezers assay. *Biophys J* 87, 1112-1135.

Pubmed: [Author and Title](#)

Google Scholar: [Author Only Title Only Author and Title](#)

Leake, M.C., Chandler, J.H., Wadhams, G.H., Bai, F., Berry, R.M., and Armitage, J.P. (2006). Stoichiometry and turnover in single, functioning membrane protein complexes. *Nature* 443, 355-358.

Pubmed: [Author and Title](#)

Google Scholar: [Author Only Title Only Author and Title](#)

Leake, M.C., Greene, N.P., Godun, R.M., Granjon, T., Buchanan, G., Chen, S., Berry, R.M., Palmer, T., and Berks, B.C. (2008). Variable stoichiometry of the TatA component of the twin-arginine protein transport system observed by in vivo single-molecule imaging. *Proc Natl Acad Sci U S A* 105, 15376-15381.

Pubmed: [Author and Title](#)

Google Scholar: [Author Only Title Only Author and Title](#)

Lenn, T., Leake, M.C., and Mullineaux, C.W. (2008). Clustering and dynamics of cytochrome bd-I complexes in the Escherichia coli plasma membrane in vivo. *Mol Microbiol* 70, 1397-1407.

Pubmed: [Author and Title](#)

Google Scholar: [Author Only Title Only Author and Title](#)

Li, Q., Yafal, A.G., Lee, Y.M., Hogle, J., and Chow, M. (1994). Poliovirus neutralization by antibodies to internal epitopes of VP4 and VP1 results from reversible exposure of these sequences at physiological temperature. *J Virol* 68, 3965-3970.

Pubmed: [Author and Title](#)

Google Scholar: [Author Only Title Only Author and Title](#)

Liberton, M., Austin, J.R., 2nd, Berg, R.H., and Pakrasi, H.B. (2011). Unique thylakoid membrane architecture of a unicellular N<sub>2</sub>-fixing cyanobacterium revealed by electron tomography. *Plant Physiol* 155, 1656-1666.

Pubmed: [Author and Title](#)

Google Scholar: [Author Only Title Only Author and Title](#)

Lin, M.T., Occhialini, A., Andralojc, P.J., Parry, M.A.J., and Hanson, M.R. (2014a). A faster Rubisco with potential to increase photosynthesis in crops. *Nature* 513, 547-550.

Pubmed: [Author and Title](#)

Google Scholar: [Author Only Title Only Author and Title](#)

Lin, M.T., Occhialini, A., Andralojc, P.J., Devonshire, J., Hines, K.M., Parry, M.A., and Hanson, M.R. (2014b).  $\beta$ -Carboxysomal proteins assemble into highly organized structures in Nicotiana chloroplasts. *Plant J* 79, 1-12.

- Pubmed: [Author and Title](#)  
Google Scholar: [Author Only Title Only Author and Title](#)
- Liu, L.N., Aartsma, T.J., Thomas, J.C., Lamers, G.E., Zhou, B.C., and Zhang, Y.Z. (2008). Watching the native supramolecular architecture of photosynthetic membrane in red algae: topography of phycobilisomes and their crowding, diverse distribution patterns. *J Biol Chem* 283, 34946-34953.  
Pubmed: [Author and Title](#)  
Google Scholar: [Author Only Title Only Author and Title](#)
- Liu, L.N., Bryan, S.J., Huang, F., Yu, J.F., Nixon, P.J., Rich, P.R., and Mullineaux, C.W. (2012). Control of electron transport routes through redox-regulated redistribution of respiratory complexes. *Proc Natl Acad Sci U S A* 109, 11431-11436.  
Pubmed: [Author and Title](#)  
Google Scholar: [Author Only Title Only Author and Title](#)
- Llorente-Garcia, I., Lenn, T., Erhardt, H., Harriman, O.L., Liu, L.N., Robson, A., Chiu, S.W., Matthews, S., Willis, N.J., Bray, C.D., Lee, S.H., Shin, J.Y., Bustamante, C., Liphardt, J., Friedrich, T., Mullineaux, C.W., and Leake, M.C. (2014). Single-molecule in vivo imaging of bacterial respiratory complexes indicates delocalized oxidative phosphorylation. *Biochim Biophys Acta* 1837, 811-824.  
Pubmed: [Author and Title](#)  
Google Scholar: [Author Only Title Only Author and Title](#)
- Long, B.M., Price, G.D., and Badger, M.R. (2005). Proteomic assessment of an established technique for carboxysome enrichment from *Synechococcus* PCC7942. *Can J Bot* 83, 746-757.  
Pubmed: [Author and Title](#)  
Google Scholar: [Author Only Title Only Author and Title](#)
- Long, B.M., Badger, M.R., Whitney, S.M., and Price, G.D. (2007). Analysis of carboxysomes from *Synechococcus* PCC7942 reveals multiple Rubisco complexes with carboxysomal proteins CcmM and CcaA. *J Biol Chem* 282, 29323-29335.  
Pubmed: [Author and Title](#)  
Google Scholar: [Author Only Title Only Author and Title](#)
- Long, B.M., Tucker, L., Badger, M.R., and Price, G.D. (2010). Functional cyanobacterial  $\beta$ -carboxysomes have an absolute requirement for both long and short forms of the CcmM protein. *Plant Physiol* 153, 285-293.  
Pubmed: [Author and Title](#)  
Google Scholar: [Author Only Title Only Author and Title](#)
- Long, B.M., Rae, B.D., Badger, M.R., and Price, G.D. (2011). Over-expression of the beta-carboxysomal CcmM protein in *Synechococcus* PCC7942 reveals a tight co-regulation of carboxysomal carbonic anhydrase (CcaA) and M58 content. *Photosynth Res* 109, 33-45.  
Pubmed: [Author and Title](#)  
Google Scholar: [Author Only Title Only Author and Title](#)
- Long, B.M., Hee, W.Y., Sharwood, R.E., Rae, B.D., Kaines, S., Lim, Y.-L., Nguyen, N.D., Massey, B., Bala, S., von Caemmerer, S., Badger, M.R., and Price, G.D. (2018). Carboxysome encapsulation of the CO<sub>2</sub>-fixing enzyme Rubisco in tobacco chloroplasts. *Nature Commun* 9, 3570.  
Pubmed: [Author and Title](#)  
Google Scholar: [Author Only Title Only Author and Title](#)
- Lund, V.A., Wacnik, K., Turner, R.D., Cotterell, B.E., Walther, C.G., Fenn, S.J., Grein, F., Wollman, A.J., Leake, M.C., Olivier, N., Cadby, A., Mesnage, S., Jones, S., and Foster, S.J. (2018). Molecular coordination of *Staphylococcus aureus* cell division. *eLife* 7, e32057.  
Pubmed: [Author and Title](#)  
Google Scholar: [Author Only Title Only Author and Title](#)
- MacCready, J.S., Hakim, P., Young, E.J., Hu, L., Liu, J., Osteryoung, K.W., Vecchiarelli, A.G., and Ducat, D.C. (2018). Protein gradients on the nucleoid position the carbon-fixing organelles of cyanobacteria. *eLife* 7, e39723.  
Pubmed: [Author and Title](#)  
Google Scholar: [Author Only Title Only Author and Title](#)
- McGinn, P.J., Price, G.D., Maleszka, R., and Badger, M.R. (2003). Inorganic carbon limitation and light control the expression of transcripts related to the CO<sub>2</sub>-concentrating mechanism in the cyanobacterium *Synechocystis* sp. strain PCC6803. *Plant Physiol* 132, 218-229.  
Pubmed: [Author and Title](#)  
Google Scholar: [Author Only Title Only Author and Title](#)
- McGurn, L.D., Moazami-Goudarzi, M., White, S.A., Suwal, T., Brar, B., Tang, J.Q., Espie, G.S., and Kimber, M.S. (2016). The structure, kinetics and interactions of the beta-carboxysomal beta-carbonic anhydrase, CcaA. *Biochem J* 473, 4559-4572.  
Pubmed: [Author and Title](#)  
Google Scholar: [Author Only Title Only Author and Title](#)
- McKay, R.M., Gibbs, S., and Espie, G. (1993). Effect of dissolved inorganic carbon on the expression of carboxysomes, localization of Rubisco and the mode of inorganic carbon transport in cells of the cyanobacterium *Synechococcus* UTEX 625. *Archives Microbiol* 159, 21-29.  
Pubmed: [Author and Title](#)  
Google Scholar: [Author Only Title Only Author and Title](#)
- Menon, B.B., Dou, Z., Heinhorst, S., Shively, J.M., and Cannon, G.C. (2008). *Halothiobacillus neapolitanus* carboxysomes sequester

heterologous and chimeric RubisCO species. *PLoS One* 3, e3570.

Pubmed: [Author and Title](#)

Google Scholar: [Author Only Title Only Author and Title](#)

Miller, H., Zhou, Z., Wollman, A.J., and Leake, M.C. (2015). Superresolution imaging of single DNA molecules using stochastic photoblinking of minor groove and intercalating dyes. *Methods* 88, 81-88.

Pubmed: [Author and Title](#)

Google Scholar: [Author Only Title Only Author and Title](#)

Miller, H., Cosgrove, J., Wollman, A.J.M., Taylor, E., Zhou, Z., O'Toole, P.J., Coles, M.C., and Leake, M.C. (2018). High-speed single-molecule tracking of CXCL13 in the B-follicle. *Front Immunol* 9, 1073.

Pubmed: [Author and Title](#)

Google Scholar: [Author Only Title Only Author and Title](#)

Niederhuber, M.J., Lambert, T.J., Yapp, C., Silver, P.A., and Polka, J.K. (2017). Superresolution microscopy of the beta-carboxysome reveals a homogeneous matrix. *Mol Biol Cell* 28, 2734-2745.

Pubmed: [Author and Title](#)

Google Scholar: [Author Only Title Only Author and Title](#)

Occhialini, A., Lin, M.T., Andralojc, P.J., Hanson, M.R., and Parry, M.A. (2016). Transgenic tobacco plants with improved cyanobacterial Rubisco expression but no extra assembly factors grow at near wild-type rates if provided with elevated CO<sub>2</sub>. *Plant J* 85, 148-160.

Pubmed: [Author and Title](#)

Google Scholar: [Author Only Title Only Author and Title](#)

Plank, M., Wadhams, G.H., and Leake, M.C. (2009). Millisecond timescale slimfield imaging and automated quantification of single fluorescent protein molecules for use in probing complex biological processes. *Integr Biol (Camb)* 1, 602-612.

Pubmed: [Author and Title](#)

Google Scholar: [Author Only Title Only Author and Title](#)

Price, G.D., and Badger, M.R. (1991). Evidence for the role of carboxysomes in the cyanobacterial CO<sub>2</sub>-concentrating mechanism. *Can J Bot* 69, 963-973.

Pubmed: [Author and Title](#)

Google Scholar: [Author Only Title Only Author and Title](#)

Rae, B.D., Long, B.M., Badger, M.R., and Price, G.D. (2012). Structural determinants of the outer shell of beta-carboxysomes in *Synechococcus elongatus* PCC 7942: roles for CcmK2, K3-K4, CcmO, and CcmL. *PLoS One* 7, e43871.

Pubmed: [Author and Title](#)

Google Scholar: [Author Only Title Only Author and Title](#)

Rae, B.D., Long, B.M., Badger, M.R., and Price, G.D. (2013). Functions, compositions, and evolution of the two types of carboxysomes: polyhedral microcompartments that facilitate CO<sub>2</sub> fixation in cyanobacteria and some proteobacteria. *Microbiol Mol Biol Rev* 77, 357-379.

Pubmed: [Author and Title](#)

Google Scholar: [Author Only Title Only Author and Title](#)

Reyes-Lamothe, R., Sherratt, D.J., and Leake, M.C. (2010). Stoichiometry and architecture of active DNA replication machinery in *Escherichia coli*. *Science* 328, 498-501.

Pubmed: [Author and Title](#)

Google Scholar: [Author Only Title Only Author and Title](#)

Ringgaard, S., van Zon, J., Howard, M., and Gerdes, K. (2009). Movement and equipositioning of plasmids by ParA filament disassembly. *Proc Natl Acad Sci U S A* 106, 19369-19374.

Pubmed: [Author and Title](#)

Google Scholar: [Author Only Title Only Author and Title](#)

Robson, A., Burrage, K., and Leake, M.C. (2013). Inferring diffusion in single live cells at the single-molecule level. *Philos Trans R Soc Lond B Biol Sci* 368, 20120029.

Pubmed: [Author and Title](#)

Google Scholar: [Author Only Title Only Author and Title](#)

Roivainen, M., Piirainen, L., Rysa, T., Narvanen, A., and Hovi, T. (1993). An immunodominant N-terminal region of VP1 protein of poliovirus that is buried in crystal structure can be exposed in solution. *Virology* 195, 762-765.

Pubmed: [Author and Title](#)

Google Scholar: [Author Only Title Only Author and Title](#)

Ryan, P., Forrester, T.J.B., Wroblewski, C., Kenney, T.M.G., Kitova, E.N., Klassen, J.S., and Kimber, M.S. (2018). The small RbcS-like domains of the beta-carboxysome structural protein, CcmM, bind RubisCO at a site distinct from that binding the RbcS subunit. *J Biol Chem*

Pubmed: [Author and Title](#)

Google Scholar: [Author Only Title Only Author and Title](#)

Saschenbrecker, S., Bracher, A., Rao, K.V., Rao, B.V., Hartl, F.U., and Hayer-Hartl, M. (2007). Structure and function of RbcX, an assembly chaperone for hexadecameric Rubisco. *Cell* 129, 1189-1200.

Pubmed: [Author and Title](#)



Google Scholar: [Author Only](#) [Title Only](#) [Author and Title](#)

**Savage, D.F., Afonso, B., Chen, A.H., and Silver, P.A. (2010). Spatially ordered dynamics of the bacterial carbon fixation machinery. *Science* 327, 1258-1261.**

Pubmed: [Author and Title](#)

Google Scholar: [Author Only](#) [Title Only](#) [Author and Title](#)

**Sbalzarini, I.F., and Koumoutsakos, P. (2005). Feature point tracking and trajectory analysis for video imaging in cell biology. *J Struct Biol* 151, 182-195.**

Pubmed: [Author and Title](#)

Google Scholar: [Author Only](#) [Title Only](#) [Author and Title](#)

**Schwarz, D., Nodop, A., Hüge, J., Purfurst, S., Forchhammer, K., Michel, K.P., Bauwe, H., Kopka, J., and Hagemann, M. (2011). Metabolic and transcriptomic phenotyping of inorganic carbon acclimation in the cyanobacterium *Synechococcus elongatus* PCC 7942. *Plant Physiol* 155, 1640-1655.**

Pubmed: [Author and Title](#)

Google Scholar: [Author Only](#) [Title Only](#) [Author and Title](#)

**Shashkova, S., and Leake, M.C. (2017). Single-molecule fluorescence microscopy review: shedding new light on old problems. *Biosci Rep* 37.**

Pubmed: [Author and Title](#)

Google Scholar: [Author Only](#) [Title Only](#) [Author and Title](#)

**Shashkova, S., Wollman, A.J., Hohmann, S., and Leake, M.C. (2018). Characterising maturation of GFP and mCherry of genomically integrated fusions in *Saccharomyces cerevisiae*. *Bio Protoc* 8, e2710.**

Pubmed: [Author and Title](#)

Google Scholar: [Author Only](#) [Title Only](#) [Author and Title](#)

**Shively, J.M., Ball, F.L., and Kline, B.W. (1973). Electron microscopy of the carboxysomes (polyhedral bodies) of *Thiobacillus neapolitanus*. *J Bacteriol* 116, 1405-1411.**

Pubmed: [Author and Title](#)

Google Scholar: [Author Only](#) [Title Only](#) [Author and Title](#)

**Sommer, M., Cai, F., Melnicki, M., and Kerfeld, C.A. (2017).  $\beta$ -Carboxysome bioinformatics: identification and evolution of new bacterial microcompartment protein gene classes and core locus constraints. *J Exp Bot* 68, 3841-3855.**

Pubmed: [Author and Title](#)

Google Scholar: [Author Only](#) [Title Only](#) [Author and Title](#)

**Sommer, M., Sutter, M., Gupta, S., Kirst, H., Turmo, A., Lechno-Yossef, S., Burton, R.L., Saechao, C., Sloan, N.B., Cheng, X., Chan, L.G., Petzold, C.J., Fuentes-Cabrera, M., Ralston, C.Y., and Kerfeld, C.A. (2019). Heterohexamers formed by CcmK3 and CcmK4 increase the complexity of beta carboxysome Shells. *Plant Physiol* 179, 156-167.**

Pubmed: [Author and Title](#)

Google Scholar: [Author Only](#) [Title Only](#) [Author and Title](#)

**Stracy, M., Wollman, A.J., Kaja, E., Gapinski, J., Lee, J.E., Leek, V.A., McKie, S.J., Mitchenall, L.A., Maxwell, A., Sherratt, D.J., Leake, M.C., and Zawadzki, P. (2018). Single-molecule imaging of DNA gyrase activity in living *Escherichia coli*. *Nucleic Acids Res* 47, 210-220.**

Pubmed: [Author and Title](#)

Google Scholar: [Author Only](#) [Title Only](#) [Author and Title](#)

**Sun, Y., Casella, S., Fang, Y., Huang, F., Faulkner, M., Barrett, S., and Liu, L.N. (2016). Light modulates the biosynthesis and organization of cyanobacterial carbon fixation machinery through photosynthetic electron flow. *Plant Physiol* 171, 530-541.**

Pubmed: [Author and Title](#)

Google Scholar: [Author Only](#) [Title Only](#) [Author and Title](#)

**Sutter, M., Faulkner, M., Aassignargues, C., Paasch, B.C., Barrett, S., Kerfeld, C.A., and Liu, L.-N. (2016). Visualization of bacterial microcompartment facet assembly using high-speed atomic force microscopy. *Nano Letters* 16, 1590-1595.**

Pubmed: [Author and Title](#)

Google Scholar: [Author Only](#) [Title Only](#) [Author and Title](#)

**Tanaka, S., Sawaya, M.R., Kerfeld, C.A., and Yeates, T.O. (2007). Structure of the RuBisCO chaperone RbcX from *Synechocystis* sp. PCC6803. *Acta crystallographica. Section D, Biological crystallography* 63, 1109-1112.**

Pubmed: [Author and Title](#)

Google Scholar: [Author Only](#) [Title Only](#) [Author and Title](#)

**Tanaka, S., Kerfeld, C.A., Sawaya, M.R., Cai, F., Heinhorst, S., Cannon, G.C., and Yeates, T.O. (2008). Atomic-level models of the bacterial carboxysome shell. *Science* 319, 1083-1086.**

Pubmed: [Author and Title](#)

Google Scholar: [Author Only](#) [Title Only](#) [Author and Title](#)

**Tinevez, J.-Y., Perry, N., Schindelin, J., Hoopes, G.M., Reynolds, G.D., Laplantine, E., Bednarek, S.Y., Shorte, S.L., and Eliceiri, K.W. (2017). TrackMate: An open and extensible platform for single-particle tracking. *Methods* 115, 80-90.**

Pubmed: [Author and Title](#)

Google Scholar: [Author Only](#) [Title Only](#) [Author and Title](#)

**Vecchiarelli, A.G., Hwang, L.C., and Mizuuchi, K. (2013). Cell-free study of F plasmid partition provides evidence for cargo transport by**

a diffusion-ratchet mechanism. *Proc Natl Acad Sci U S A* 110, E1390-1397.

Pubmed: [Author and Title](#)

Google Scholar: [Author Only](#) [Title Only](#) [Author and Title](#)

Wang, H., Yan, X., Aigner, H., Bracher, A., Nguyen, N.D., Hee, W.Y., Long, B.M., Price, G.D., Hartl, F.U., and Hayer-Hartl, M. (2019). Rubisco condensate formation by CcmM in beta-carboxysome biogenesis. *Nature* 566, 131-135.

Pubmed: [Author and Title](#)

Google Scholar: [Author Only](#) [Title Only](#) [Author and Title](#)

Whitehead, L., Long, B.M., Price, G.D., and Badger, M.R. (2014). Comparing the in vivo function of alpha-carboxysomes and beta-carboxysomes in two model cyanobacteria. *Plant Physiol* 165, 398-411.

Pubmed: [Author and Title](#)

Google Scholar: [Author Only](#) [Title Only](#) [Author and Title](#)

Wollman, A.J., and Leake, M.C. (2015). Millisecond single-molecule localization microscopy combined with convolution analysis and automated image segmentation to determine protein concentrations in complexly structured, functional cells, one cell at a time. *Faraday Discuss* 184, 401-424.

Pubmed: [Author and Title](#)

Google Scholar: [Author Only](#) [Title Only](#) [Author and Title](#)

Wollman, A.J., and Leake, M.C. (2016). Single-molecule narrow-field microscopy of protein-DNA binding dynamics in glucose signal transduction of live yeast cells. *Methods Mol Biol* 1431, 5-15.

Pubmed: [Author and Title](#)

Google Scholar: [Author Only](#) [Title Only](#) [Author and Title](#)

Wollman, A.J., Miller, H., Foster, S., and Leake, M.C. (2016a). An automated image analysis framework for segmentation and division plane detection of single live *Staphylococcus aureus* cells which can operate at millisecond sampling time scales using bespoke Slimfield microscopy. *Physical Biol* 13, 055002.

Pubmed: [Author and Title](#)

Google Scholar: [Author Only](#) [Title Only](#) [Author and Title](#)

Wollman, A.J., Syeda, A.H., McGlynn, P., and Leake, M.C. (2016b). Single-molecule observation of DNA replication repair pathways in *E. coli*. *Adv Exp Med Biol* 915, 5-16.

Pubmed: [Author and Title](#)

Google Scholar: [Author Only](#) [Title Only](#) [Author and Title](#)

Wollman, A.J., Shashkova, S., Hedlund, E.G., Friemann, R., Hohmann, S., and Leake, M.C. (2017). Transcription factor clusters regulate genes in eukaryotic cells. *eLife* 6, e27451.

Pubmed: [Author and Title](#)

Google Scholar: [Author Only](#) [Title Only](#) [Author and Title](#)

Woodger, F.J., Badger, M.R., and Price, G.D. (2003). Inorganic carbon limitation induces transcripts encoding components of the CO<sub>2</sub>-concentrating mechanism in *Synechococcus* sp. PCC7942 through a redox-independent pathway. *Plant Physiol* 133, 2069-2080.

Pubmed: [Author and Title](#)

Google Scholar: [Author Only](#) [Title Only](#) [Author and Title](#)

Yeates, T.O., Crowley, C.S., and Tanaka, S. (2010). Bacterial microcompartment organelles: protein shell structure and evolution. *Annual Rev Biophys* 39, 185-205.

Pubmed: [Author and Title](#)

Google Scholar: [Author Only](#) [Title Only](#) [Author and Title](#)